

## PHOTOIONIZATION DYNAMICS OF SMALL MOLECULES

J. L. Dehmer

Argonne National Laboratory  
Argonne, IL 60439, USA

Dan Dill

Department of Chemistry  
Boston University  
Boston, MA 02215, USA

A. C. Parr

Synchrotron Ultraviolet Radiation Facility  
National Bureau of Standards  
Washington, D.C. 20234, USA

### 1. INTRODUCTION

The last decade has witnessed remarkable progress in characterizing dynamical aspects of the molecular photoionization process. The general challenge is to gain physical insight into those processes occurring during photoexcitation and eventual escape of the photoelectron through the anisotropic molecular field, in terms of various observables such as photoionization cross-sections and branching ratios, photoelectron angular distributions and even newer probes mentioned below. Much of the progress in this field has mirrored earlier work in atomic photoionization dynamics [1] where many key ideas were developed (e.g., channel interaction, quantum defect analysis, potential barrier phenomena and experimental techniques). However, additional concepts and techniques were required to deal with the strictly molecular aspects of the problem, particularly the anisotropy of the multicenter molecular field and the interaction among rovibronic modes.

From among the great variety of successful approaches to the study of molecular photoionization dynamics, one can identify four broad classes which together form the core of recent activities in this field: *First*, the extensive measurements of total photoionization cross-sections from the VUV to the x-ray range by a variety of means (see, e.g., [2,3] and original literature cited below) have continuously provided fresh impetus to account for a variety of phenomena displayed in molecular oscillator strength distributions. *Second*, in response to observations [4-17] of broad, intense features in photoionization spectra of small molecules, the interpretation and study of shape resonances in molecular photoionization began [18-32] and grew into a sizable subfield [33-134]. Benefitting greatly from the timely development of realistic, independent-electron models [67,94,123,135,136] for molecular photoionization, studies in this area not only accounted for the features in the total photoionization spectra, but also established and predicted several manifestations in other physical observables as discussed below. *Third*, multichannel quantum defect theory (MQDT) was adapted [137-150] to molecular photoionization, thus providing a framework for the quantitative and microscopic analysis of autoionization phenomena. This powerful theoretical framework has been successfully applied to a number of prototypical diatomic molecules, yielding both insight into detailed dynamics of resonant photoionization and some specific predictions for experimental testing by means discussed in the next item. *Fourth*, technical advances, especially the development of intense synchrotron radiation sources [151-156], have made it feasible to perform triply-differential photoionization measurements (see, e.g., [75, 157-163]) on gas-phase atoms and molecules. By "triply-differential" we mean that photoelectron measurements are made as a function of three independent variables -- incident photon wavelength, photoelectron energy and photoelectron ejection angle. Variable wavelength permits the study of photoionization at and within spectral features of interest; photoelectron energy analysis permits separation and selection of individual (ro)vibronic ionization channels; and measurement of photoelectron angular distributions accesses dynamical information (i.e., relative phases of alternative, degenerate ionization channels) not present in integrated cross-sections. This level of experimental detail approaches that at which theoretical calculations are made and, hence, permits us to isolate and study dynamical details which are otherwise swamped in integrated or averaged quantities. We emphasize that, although the current trend is toward the use of synchrotron radiation for variable-wavelength studies, a variety of light sources have been successfully used to study photoionization dynamics. For example, in the shape-resonance literature cited above, many of the pioneering measurements were carried out with laboratory-scale sources. Likewise, although most current measurements of vibrational branch-

ing ratios [132-134,164-170] and angular distributions [166-170] within autoionizing resonances employ synchrotron radiation, many early and ongoing studies with traditional light sources have made significant observations of the effects of autoionization on vibrational branching ratios [171-183] and angular distributions [175,184-193].

In this paper we review the recent progress outlined above, with emphasis on photoionization dynamics exhibited by shape and autoionizing resonance phenomena. Prototypes, such as  $H_2$  and  $N_2$ , will be used in order to best illustrate the fundamental aspects and the variety of manifestations of these processes. Finally, in Section 4, we present an overview of several other approaches to the study of molecular photoionization dynamics in order to show how they complement those topics emphasized here and to convey, to some extent, the richness of the field.

## 2. SHAPE RESONANCES IN MOLECULAR PHOTOIONIZATION

### 2.1 Overview

Shape resonances are quasibound states in which a particle is temporarily trapped by a potential barrier, through which it may eventually tunnel and escape. In molecular fields, such states can result from so-called "centrifugal barriers", which block the motion of otherwise free electrons in certain directions, trapping them in a region of space with molecular dimensions. Over the past few years, this basic resonance mechanism has been found to play a prominent role in a variety of processes in molecular physics, most notably in photoionization and electron scattering. As discussed more fully in later sections, the expanding interest in shape-resonant phenomena arises from a few key factors:

*First*, shape resonance effects are being identified in the spectra of a growing and diverse collection of molecules and now appear to be active somewhere in the observable properties of most small (nonhydride) molecules. Examples of those processes which exhibit shape resonance effects are x-ray and VUV absorption spectra, photoelectron branching ratios and photoelectron angular distributions (including those vibrationally resolved), Auger-electron angular distributions [82], elastic electron scattering [194-196], vibrational excitation by electron impact [81,195-196], and so on. Thus, concepts and techniques developed in this connection can be used extensively in molecular physics.

*Second*, being quasibound inside a potential barrier on the

perimeter of the molecule, shape resonances are localized, have enhanced electron density in the molecular core, and are uncoupled from the external environment of the molecule. This localization often produces intense, easily studied spectral features, while suppressing the nearby continuum and/or Rydberg structure and, as discussed more fully below, has a marked influence on vibrational motion. In addition, localization causes much of the conceptual framework developed for shape resonances in free molecules to apply equally well [68] to photoionization and electron scattering, and to other states of matter such as adsorbed molecules [29,31,197-198], molecular crystals [11,20] and ionic solids [199].

*Third*, resonant trapping by a centrifugal barrier often imparts a well-defined orbital momentum character to the escaping electron. This can be directly observed (e.g., by angular distributions of scattered electrons [194-196] or photoelectron angular distributions from oriented molecules [29,31,197,198]) and shows that the centrifugal-trapping mechanism has physical meaning and is not merely a theoretical construct. Recent case studies have revealed trapping of  $\ell = 1$  to  $\ell = 5$  components of continuum molecular wave functions. The purely molecular origin of the great majority of these cases is illustrated by the  $N_2$  prototype discussed in Section 2.2.

*Fourth*, the predominantly one-electron nature of the phenomenon lends itself to theoretical treatment by realistic, independent-electron methods [67,94,123,135-136], with the concomitant flexibility in terms of complexity of molecular systems, energy ranges and alternative physical processes. This has been a major factor in the rapid exploration of this area. Continuing development of computational schemes holds the promise of elevating the level of theoretical work on molecular ionization and scattering in order to test and quantify the independent-particle results and to treat other circumstances such as weak channels, multiply-excited states, etc., where the simpler schemes become invalid.

The earliest, and still possibly the most dramatic, examples of shape resonance effects in molecules are the photoabsorption spectra of the sulfur K- [4,14a] and L-shells [5,8,11,14a] in  $SF_6$ . The sulfur L-shell absorption spectra of  $SF_6$  and  $H_2S$ , shown in Fig. 1, illustrate the types of phenomena that originally drew attention to this area. In Fig. 1, both spectra are plotted on a photon energy scale referenced to the sulfur L-shell ionization potential (IP), which is chemically shifted by a few eV in the two molecular environments but which lies near  $h\nu \approx 175$  eV. The ordinates represent relative photoabsorption cross-sections and have been adjusted so that the integrated oscillator strength for the two systems is roughly equal in this

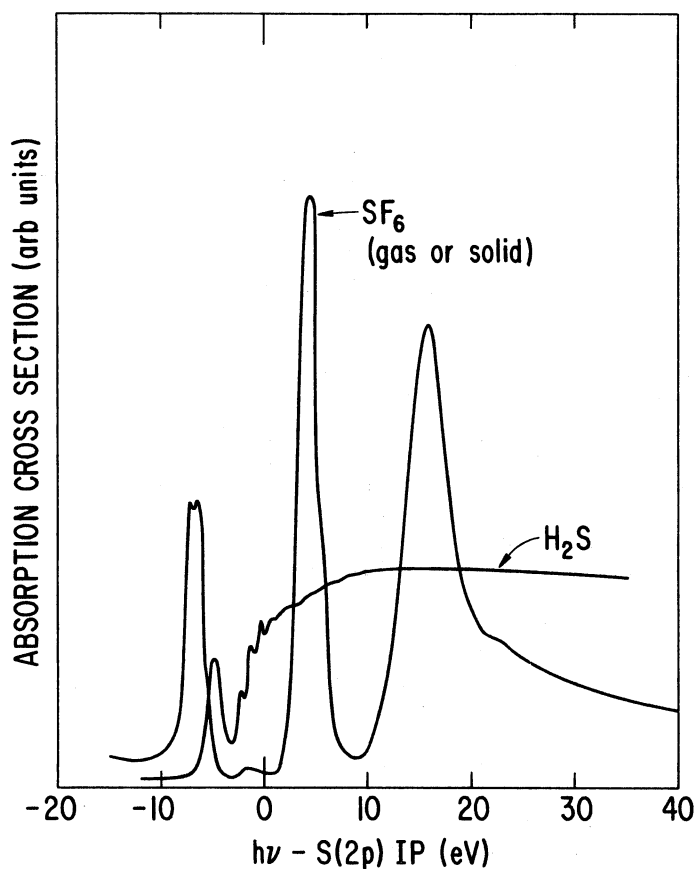


Fig. 1. Photoabsorption spectra of  $\text{H}_2\text{S}$  (adapted from [8]) and  $\text{SF}_6$  (adapted from [11]) near the sulfur  $L_{2,3}$  edge.

spectral range (absolute calibrations are not known). The  $\text{H}_2\text{S}$  spectrum is used here as a "normal" reference spectrum since hydrogen atoms normally do not contribute appreciably to shape resonance effects and, in this particular context, can be regarded as weak perturbations on the inner-shell spectra of the heavy atom. Indeed, the photoabsorption spectrum exhibits a valence transition, followed by partially resolved Rydberg structure which converges to a smooth continuum. The gradual rise at threshold is attributable to the delayed onset of the " $2p \rightarrow \epsilon d$ " continuum which, for second-row atoms, will exhibit a delayed onset prior to the occupation of the 3d subshell. This is the qualitative behavior one might well expect for the absorption spectrum of a core level.

In sharp contrast to this, the photoabsorption spectrum of the same sulfur 2p subshell in  $\text{SF}_6$  shows no vestige of the "normal" behavior just described. Instead, three intense, broad peaks appear, one below the ionization threshold and two above, and the continuum absorption cross-section is greatly reduced elsewhere. Moreover, no Rydberg structure is apparent although an infinite number of Rydberg states must necessarily be associated with any molecular ion. (Actually, Rydberg states were detected [33], using photographic methods, superimposed on the weak bump below the IP; obviously, however, these states are extremely weak in this spectrum.) This radical reorganization of the oscillator strength distribution has been interpreted [20] in terms of potential barrier effects in  $\text{SF}_6$ , resulting in three shape-resonantly enhanced final-state features of  $a_{1g}$ ,  $t_{2g}$  and  $e_g$  symmetry (in order of increasing energy). Another shape-resonant feature ( $t_{1u}$  symmetry) is prominent in the sulfur K-shell spectrum [4] and, in fact, is responsible, via channel interactions, for the weak feature just below the IP in Fig. 1. Hence, four prominent features occur in the photoexcitation spectrum of  $\text{SF}_6$  as a consequence of potential barriers caused by the molecular environment of the sulfur atom. Another significant observation [11] is that the  $\text{SF}_6$  curve in Fig. 1 represents both gaseous and solid  $\text{SF}_6$ , within experimental error bars. This is definitive evidence that the resonances are eigenfunctions of the potential well inside the barrier and are effectively uncoupled from the molecule's external environment.

In what follows, we describe the underlying physics of shape resonances in molecular fields and go on to discuss several other manifestations of this phenomenon, manifestations which have been brought to light since the initial interpretation [20] of the features in Fig. 1.

## 2.2 Basic Properties

The central concept in shape resonance phenomena is the single-channel, barrier-penetration model familiar from introductory quantum mechanics. In fact, the name "shape resonance" means simply that the resonance behavior arises from the "shape" (i.e., the barrier and associated inner and outer wells) of a local potential. The basic shape resonance mechanism is illustrated schematically [200] in Fig. 2. There, an effective potential for an excited and/or unbound electron is shown to have an inner well at small distances, a potential barrier at intermediate distances and an outer well (asymptotic form not shown) at large separations. In the context of molecular photoionization, this would be a one-dimensional abstraction of the effective potential for the photoelectron in the field of a molecular ion. Accordingly, the inner well would be formed by the partially screened nuclei in the molecular core and would therefore be

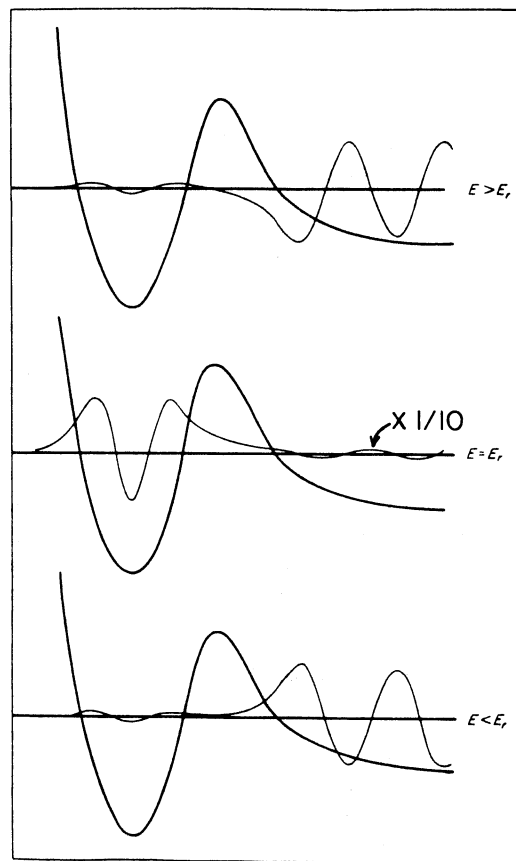


Fig. 2. Schematic of the effect of a potential barrier on an unbound wavefunction in the vicinity of a quasibound state at  $E = E_r$  (adapted from [200]). In the present context, the horizontal axis represents the distance of the excited electron from the center of the molecule.

highly anisotropic and would overlap much of the molecular charge distribution (i.e., the initial states of the photoionization process). The barrier, in all well-documented cases, is a so-called centrifugal barrier (other forces such as repulsive exchange forces, high concentrations of negative charge, etc. may also contribute, but have not yet been documented to be pivotal in the molecular systems studied to date). This centrifugal barrier derives from a competition between repulsive centrifugal forces and attractive electrostatic forces and usually resides on the perimeter of the molecular charge distribution where the centrifugal forces can compete effectively with elec-

trostatic forces. Similar barriers are known for d and f waves in atomic fields [1]; however, the  $\ell$  (orbital angular momentum) character of resonances in molecular fields tends to be higher than those of constituent atoms owing to the larger spatial extent of the molecular charge distribution (e.g., see the discussion given below in connection with  $N_2$  photoionization). The outer well lies outside the molecule where the Coulomb potential ( $\sim r^{-1}$ ) of the molecular ion again dominates the centrifugal terms ( $\sim r^{-2}$ ) in the potential. We stress that this description has been radically simplified to convey the essential aspects of the underlying physics. In reality, effective barriers to electron motion in molecular fields occur for particular  $\ell$  components of particular ionization channels and restrict motion only in certain directions. Again, a specific example is described below.

Focusing now on the wavefunctions in Fig. 2, we see the effect of the potential barrier on the wave mechanics of the photoelectron. For energies below the resonance energy  $E < E_r$  (lower part of Fig. 2), the inner well does not support a quasibound state (i.e., the wave function is not exponentially decaying as it enters the classically forbidden region of the barrier). Thus, the wavefunction begins to diverge in the barrier region and emerges in the outer well with a much larger amplitude than that in the inner well. When properly normalized at large  $r$ , the amplitude in the molecular core is very small; hence, we say this wavefunction is essentially an eigenfunction of the outer well although small precursor loops extend inside the barrier into the molecular core.

At  $E = E_r$ , the inner well supports a quasibound state. The wavefunction exhibits exponential decay in the barrier region so that if the barrier extended to  $r \rightarrow \infty$ , a true bound state would lie very near this total energy. Therefore, the antinode that was not supported in the inner well at  $E < E_r$  has traversed the barrier to become part of a quasibound waveform which decays monotonically until it reemerges in the outer-well region, much diminished in amplitude. This "barrier penetration" by an antinode produces a rapid increase in the asymptotic phase shift by  $\sim \pi$  radians and greatly enhances the amplitude in the inner well over a narrow band of energy near  $E_r$ . Therefore, at  $E = E_r$  the wavefunction is essentially an eigenfunction of the inner well although it decays through the barrier and reemerges in the outer well. The energy halfwidth of the resonance is related to the lifetime of the quasibound state and to the energy derivative of the rise in the phase shift in well-known ways. Finally, for  $E > E_r$  the wavefunction reverts to being an eigenfunction of the outer well since the behavior of the wavefunction at the outer edge of the inner well is no longer characteristic of a bound state.

Obviously, this resonant behavior will cause significant physical effects: The enhancement of the inner-well amplitude at  $E \approx E_r$  results in good overlap with the initial states, which reside mainly in the inner well. Conversely, for energies below the top of the barrier but not within the resonance halfwidth of  $E_r$ , the inner amplitude is diminished relative to a more typical barrier-free case. This accounts for the strong modulation of the oscillator strength distribution in Fig. 1. Also, the rapid rise in the phase shift induces shape resonance effects in the photoelectron angular distribution. Another important aspect is that eigenfunctions of the inner well are localized inside the barrier and are substantially uncoupled from the external environment of the molecule. As mentioned above, this means that shape-resonant phenomena often persist in going from the gas phase to the condensed phase (cf., Fig. 1) and, with suitable modification, shape resonances in molecular photoionization can be mapped [68] into electron-scattering processes and vice versa. Finally, note that this discussion was focused on total energies, measured from the bottom of the outer well to the top of the barrier, and that no explicit mention was made of the asymptotic potential that determines the threshold for ionization. Thus, valence or Rydberg states in this range can also exhibit shape-resonant enhancement, even though they have true bound state behavior at large  $r$ , beyond the outer well.

We now turn, for the remainder of this section, to the specific example of the well-known  $\sigma_u$  shape resonance in  $N_2$  photoionization, which was the first documented case [28] in a diatomic molecule and has since been used as a prototype in studies of various shape resonance effects. To identify the major final-state features in  $N_2$  photoionization at the independent-electron level, we show (Fig. 3) the original calculation [28-30] of the K-shell photoionization spectrum, performed with the multiple-scattering model. This calculation agrees qualitatively, with all major features in the experimental spectrum [13,44,87], except for a narrow band of double excitation features, and with subsequent, somewhat more accurate, calculations using  $L^2$  techniques [47]. The four partial cross-sections in Fig. 3 represent the four dipole-allowed channels for K-shell (IP = 409.9 eV) photoionization. Here, we have neglected the localization [54] of the K-shell hole, since it does not greatly affect the integrated cross-sections, and the separation into u and g symmetry both helps the present discussion and is rigorously applicable to the subsequent discussion of valence-shell excitation. (Note that the identification of shape-resonant behavior is generally easier in inner-shell spectra since the problems of overlapping spectra, channel interaction and zeros in the dipole matrix element are all reduced relative to valence-shell spectra.)

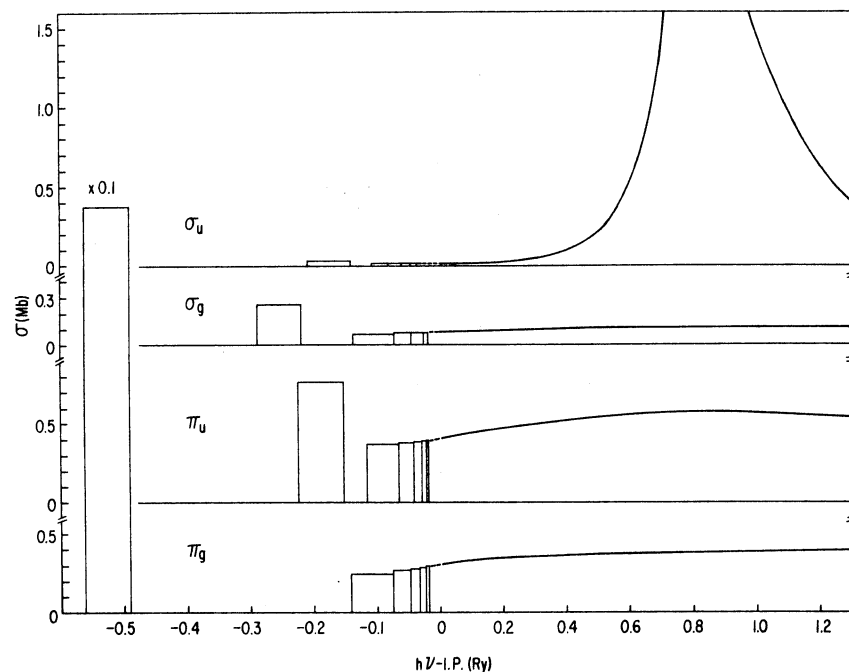


Fig. 3. Partial photoionization cross-sections for the four dipole-allowed channels in K-shell photoionization of  $N_2$ . Note that the energy scale is referenced to the K-shell IP (409.9 eV) and is expanded two-fold in the discrete part of the spectrum.

The most striking spectral feature in Fig. 3 is the first member of the  $\pi_g$  sequence, which dominates every other feature in the theoretical spectrum by a factor of  $\sim 30$ . (Note that the first  $\pi_g$  peak has been reduced by a factor of 10 in order to fit in the frame.) The concentration of oscillator strength in this peak is a centrifugal-barrier effect in the d-wave component of the  $\pi_g$  wavefunction. The final state in this transition is a highly localized state, about the size of the molecular core, and is the counterpart of the well-known [195, 196]  $\pi_g$  shape resonance in  $e-N_2$  scattering at 2.4 eV. For the latter case, Krauss and Mies [201] demonstrated that the effective potential for the  $\pi_g$  elastic channel in  $e-N_2$  scattering exhibits a potential barrier resulting from the centrifugal repulsion acting on the dominant  $\ell = 2$  lead term in the partial-wave expansion of the  $\pi_g$  wavefunction. In the case of  $N_2$  photoionization, there is one less electron in the molecular field to screen the nuclear charge so that this resonance feature is shifted [68] to lower energy and appears in the discrete region of the spectrum. It is in this sense that we refer to such fea-

tures as "discrete" shape resonances. The remainder of the  $\pi_g$  partial cross-section consists of a Rydberg series and a flat continuum. The  $\pi_u$  and  $\sigma_g$  channels both exhibit Rydberg series, the initial members of which correlate well with partially resolved transitions in the experimental spectrum below the K-shell IP.

The  $\sigma_u$  partial cross-section, on the other hand, was found to exhibit behavior rather unexpected for the K-shell of a first-row diatomic. Its Rydberg series was extremely weak and an intense, broad peak appeared at  $\sim 1$  Ry above the IP in the low-energy continuum. This effect is caused by a centrifugal barrier acting on the  $\ell = 3$  component of the  $\sigma_u$  wavefunction. The essence of the phenomenon can be described in mechanistic terms as follows: The electric-dipole interaction, localized within the atomic K shell, produces a photoelectron with angular momentum  $\ell = 1$ . As this p wave escapes to infinity, the anisotropic molecular field can scatter it into the entire range of angular momentum states contributing to the allowed  $\sigma$ - and  $\pi$ -ionization channels ( $\Delta\ell = 0, \pm 1$ ). In addition, the spatial extent of the molecular field, consisting of two atoms separated by 1.1 Å, enables the  $\ell = 3$  component of the  $\sigma_u$  continuum wavefunction to overcome its centrifugal barrier and to penetrate into the molecular core at a kinetic energy of  $\sim 1$  Ry. This penetration is rapid, with a phase shift of  $\sim \pi$  occurring over a range of  $\sim 0.3$  Ry. These two circumstances combine to produce a dramatic enhancement of photoelectron current at  $\sim 1$  Ry kinetic energy, with predominantly f-wave character.

The specifically molecular character of this phenomenon is emphasized by comparison with K-shell photoionization in atomic nitrogen and in the united-atom case, silicon. In contrast to  $N_2$ , there is no mechanism for the essential p-f coupling and neither atomic field is strong enough to support resonant penetration of high- $\ell$  partial waves through their centrifugal barriers. (With substitution of "d" for "f", this argument applies equally well to the d-type resonance in the discrete part of the spectrum.) Note that the  $\pi_u$  channel also has an  $\ell = 3$  component but does not resonate. This underscores the directionality and symmetry dependence of the trapping mechanism.

To place the  $\sigma_u$  resonance in a broader perspective and to show its connection with high-energy behavior, we present, in Fig. 4, an extension of the calculation of Fig. 3 to much higher energy. Again, the four dipole-allowed channels in  $D_{\infty h}$  symmetry are shown. The dashed line is two times the atomic nitrogen K-shell cross-section. Note that the modulation about the atomic cross-section, caused by the potential barrier, extends to  $\sim 100$  eV above threshold before the molecular and atomic curves seem to coalesce.

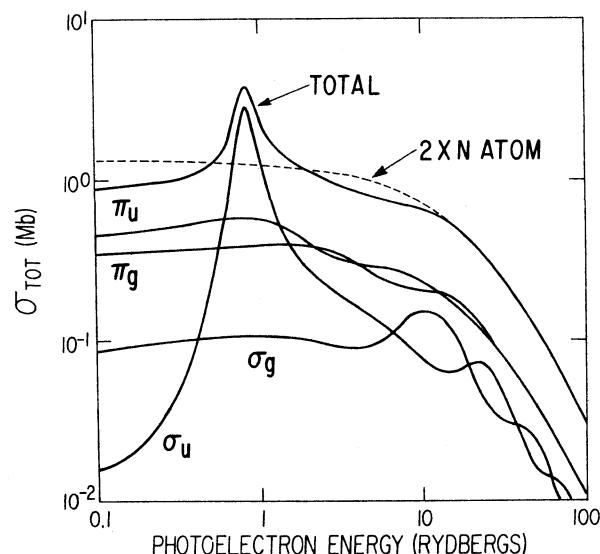


Fig. 4. Partial photoionization cross-sections for the K shell of  $N_2$  over a broad energy range. The dashed line represents twice the K-shell photoionization cross-section for atomic nitrogen, as represented by a Hartree-Slater potential.

At higher energies, a weaker modulation appears in each partial cross-section. This weak modulation is a diffraction pattern, resulting from scattering of the photoelectron by the neighboring atom in the molecule, or, more precisely, by the molecular field. Structure of this type was first studied over 50 years ago by Kronig [202] in the context of metal lattices. It currently goes by the acronym EXAFS (extended x-ray absorption fine structure) and is used extensively [151,152] for local structure determination in molecules, solids and surfaces. The net oscillation is very weak in  $N_2$  since the light atom is a weak scatterer. More pronounced effects are seen, for example, in K-shell spectra [203] of  $Br_2$  and  $GeCl_4$ . Our reason for showing the weak EXAFS structure in  $N_2$  is to emphasize that the low-energy resonant modulation (called "near-edge" structure in the context of EXAFS) and high-energy EXAFS evolve continuously into one another and emerge naturally from a single molecular framework, although high-energy EXAFS is usually treated from an atomic point of view.

Fig. 5 shows a hypothetical experiment which clearly demonstrates the  $\ell$  character of the  $\sigma_u$  resonance. In this experiment, we first fix the nitrogen molecule in space and orient the

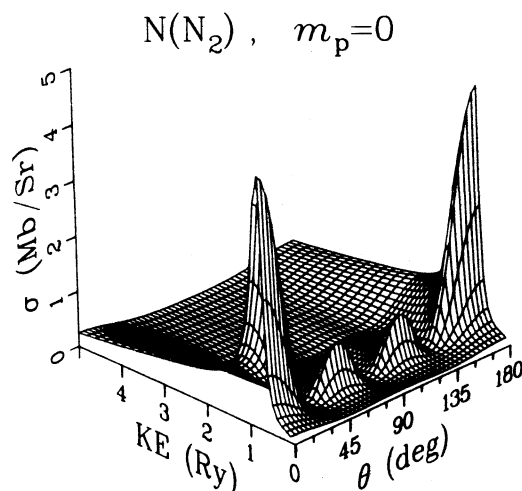


Fig. 5. Fixed-molecule photoelectron angular distribution for kinetic energies 0-5 Ry above the K-shell IP of  $N_2$ . The polarization of the ionizing radiation is oriented along the molecular axis in order to excite the  $\sigma$  continua; and the photoelectron ejection angle,  $\theta$ , is measured relative to the molecular axis.

polarization direction of a photon beam, tuned near the nitrogen K edge, along the molecular axis. This orientation will cause photoexcitation into  $\sigma$  final states, including the resonant  $\sigma_u$  ionization channel. Fig. 5 shows the angular distribution of photocurrent as a function of both excess energy above the K-shell IP and angle of ejection  $\theta$ , relative to the molecular axis. The enhanced photocurrent at the resonance position,  $KE \approx 1$  Ry, is very apparent in Fig. 5. Moreover, the angular distribution exhibits three nodes, with most of the photocurrent exiting the molecule along the molecular axis and none at right angles to it. This is an f-wave ( $\ell = 3$ ) pattern and clearly indicates that the resonant enhancement is caused by an  $\ell = 3$  centrifugal barrier in the  $\sigma_u$  continuum of  $N_2$ . Thus, the centrifugal barrier has observable physical meaning and is not merely a theoretical construct. Note that the correspondence between the dominant, asymptotic partial wave and the trapping mechanism is not always valid, especially when the trapping is on an internal or off-center atomic site where the trapped partial wave can be scattered by the anisotropic molecular field into alternative asymptotic partial waves, as is the case in, for example,  $BF_3$  [114] and  $SF_6$ . Finally, note that the hypothetical experiment discussed above has been approximately realized by photoionizing molecules adsorbed on surfaces. The shape-re-

sonant features tend to survive adsorption and, owing to their observable  $\ell$  character, can even provide evidence [197,198] as to the orientation of the molecule on the surface.

The final topic in the discussion of basic properties of shape resonances involves eigenchannel contour maps [107], or, "pictures" of unbound electrons. This is the continuum counterpart of contour maps of bound-state electronic wavefunctions, maps which have proven so valuable as tools in quantum-chemical visualization and analysis. Indeed, the present example helps achieve a physical picture of the  $\sigma_u$  shape resonance and the general technique promises to be a useful tool for future analyses of resonant trapping mechanisms and other observable properties. The key to this visualization (given in Eq. (5) below) is the construction of those particular combinations of continuum orbital momenta that diagonalize the interaction of the unbound electron with the anisotropic molecular field. These combinations, known as eigenchannels, are the continuum analogues of the eigenstates in the discrete spectrum (i.e., the bound states).

The electronic eigenvalue problem in the molecular continuum is inhomogeneous --- that is, there is a solution at every energy. Moreover, there are, in general, alternative solutions possible at a given energy, depending upon how the inhomogeneity is chosen. Typically, calculations are done in terms of real, oscillatory radial functions for the alternative possible orbital momenta. The result is the K-matrix normalized partial-wave expansion of the continuum electronic wavefunction, which takes the asymptotic form [67,135,204]

$$\psi_L \sim (\pi k)^{-1/2} r^{-1} \sum_{L'} [\sin \theta_{\ell} \delta_{LL'} + K_{LL'} \cos \theta_{\ell}] Y_{L'}(\hat{r}) \quad (1)$$

where  $L=(\ell, m)$ , the photoelectron orbital momentum and its projection along the molecular  $z$  axis;  $k^2$  is the electron kinetic energy in Rydbergs; the electron distance  $r$  from the molecular center is in Bohrs;  $\theta_{\ell} = kr - \ell(\pi/2) + \omega$ , where the Coulomb phase  $\omega = -(Z/k) \ln(2kr) + \arg \Gamma[\ell+1-i(Z/k)]$ ; molecular-ion charge is  $Z=1$ . The coefficients  $K_{LL'}$  of the cosine terms form a real, symmetric matrix known as the K matrix. The K matrix tells us about the coupling, due to the nonspherical molecular potential, between different angular momenta and, as such, summarizes the electron-molecule interaction in a compact way. That single orbital momentum  $L$  (we refer here to  $\ell$  and  $m$  collectively as orbital momentum) for which there occurs a sine term specifies the inhomogeneity, and each choice of  $L$  gives a row of the K matrix. By determining all rows in this way, we obtain the full K matrix and thereby a complete set of functions at the given energy.

The wavefunction (1) specifies what might be called a calculational boundary condition. Its form allows us to obtain the K-matrix while working in terms of real radial functions. There are two other types of boundary conditions [67,135,204], however-- physical boundary conditions, appropriate for representing physical observables, and eigenchannel boundary conditions, appropriate for analysis of the continuum wavefunction itself. The sets of wavefunctions for these alternative three types of boundary conditions are interrelated by unitary transformations.

Physical boundary conditions are introduced to obtain physical observables. One transforms to complex radial functions so that the directional character of the continuum electron at large distances, where it is detected, can be represented. This so-called S-matrix boundary condition, and its use in representing electron-molecule scattering and molecular photoionization, is discussed, for example, in [67,135].

Physical boundary conditions, however, are not well-suited to analysis of the continuum wavefunction itself. What is needed, rather, are the "normal modes" of the interaction of the continuum electron with the molecule --- that is, the eigenchannels of the electron-molecule complex. These are obtained by diagonalizing the K-matrix

$$\tan(\pi\mu_\alpha)\delta_{\alpha\alpha'} = \sum_{LL'} U_{\alpha L} K_{LL'} U_{L'\alpha'} \quad (2)$$

to give the eigenvectors  $\Psi_\alpha$  and eigenphases  $\mu_\alpha$ . The coefficients  $U_{L\alpha}$  give the composition of the alternative eigenvectors  $\Psi_\alpha$  in terms of the K-matrix-normalized functions  $\Psi_L$ :

$$\Psi_\alpha = \sum_L \Psi_L U_{L\alpha} \quad (3)$$

Using Eq. (2) and the fact that the matrix U is unitary,

$$\delta_{LL'} = \sum_\alpha U_{L\alpha} U_{\alpha L'} \quad (4)$$

we can rewrite the eigenvectors as [204]

$$\Psi_\alpha \sim (\pi k)^{-1/2} r^{-1} \sum_L [\sin\theta_L + \tan(\pi\mu_\alpha) \cos\theta_L] Y_L(\hat{r}) U_{L\alpha} \quad (5)$$

Eq. (5) is the key result of this discussion. Because molecules are not spherical, an electron of a particular angular momentum is, in general, "rescattered" into a range of angular momenta. This rescattering is indicated in Eq. (1) by the sum over  $L'$ , and the coefficients  $K_{LL'}$  give the relative amplitudes of the various rescatterings. The eigenchannel functions (5), on the other hand, correspond to those special combinations of incident angular momenta which are unchanged by the anisotropic potential of the molecule, i.e., the normal (eigen) modes of the

electron-molecule interaction.

Comparison of Eq. (5) with Eq. (1), then, shows why the eigenchannel representation (5) is more suitable for analysis of the continuum molecular electronic wavefunction: First, as we have seen, the mixing of different orbital momenta is greatly simplified. Second, the radial wavefunctions for different angular momenta all have the same mixing coefficient  $\tan(\pi\mu_\alpha)$ . Third, if an eigenchannel is dominated by a particular orbital momentum, the eigenchannel wavefunction (5) has the characteristic angular pattern of the corresponding spherical harmonic. Last, and perhaps most important, because quasibound, shape-resonant states generally resonate in a single eigenchannel  $\alpha$ , the eigenchannel representation gives us the most direct image of these resonant states.

As discussed earlier, the  $\sigma_u$  resonance is accompanied by a corresponding rise by  $\sim\pi$  radians in one component of the eigenphase sum

$$\mu_{\text{sum}} = \sum_{\alpha} \mu_{\alpha} \quad (6)$$

This resonant component, in turn, consists almost entirely of the single partial wave  $\ell = 3$ ,

$$U_{L\alpha_{\text{res}}} \approx \delta_{\ell 3} \quad (7)$$

At these kinetic energies only one other orbital momentum,  $\ell = 1$ , contributes appreciably to the photoelectron wavefunction. (Orbital momenta  $\ell = 0, 2, 4$ , etc. do not contribute because they are of even parity, and  $\ell = 5$  and higher odd orbital momenta are kept away from the molecule by their centrifugal barriers.) This means that there is only one other appreciable eigenchannel. The eigenphase component of this channel, primarily  $\ell = 1$ , is nearly constant throughout the resonant region. Thus, within about 20 eV above the ionization threshold, the  $N_2$  odd-parity continuum can be analyzed in terms of just two eigenchannels, a nonresonant p-like channel and a resonant f-like one.

In Fig. 6, we have plotted the p-like eigenchannel wavefunction for two kinetic energies, one before (top) and one at (bottom) the resonance, which in this calculation falls at  $\sim 1.2$  Ry. The molecule is in the yz plane, along the z axis. The surface contours have been projected onto the plane to show more clearly the angular variation of the wavefunction. The single nodal plane characteristic of p waves is clearly seen in this projection. It is remarkable that, despite the complex  $\ell$ -mixing induced by the anisotropic molecular potential, this eigenchannel has such a well-defined ( $\ell = 1$ ) orbital momentum character. We stress, however, that such emergence of a single orbital momen-

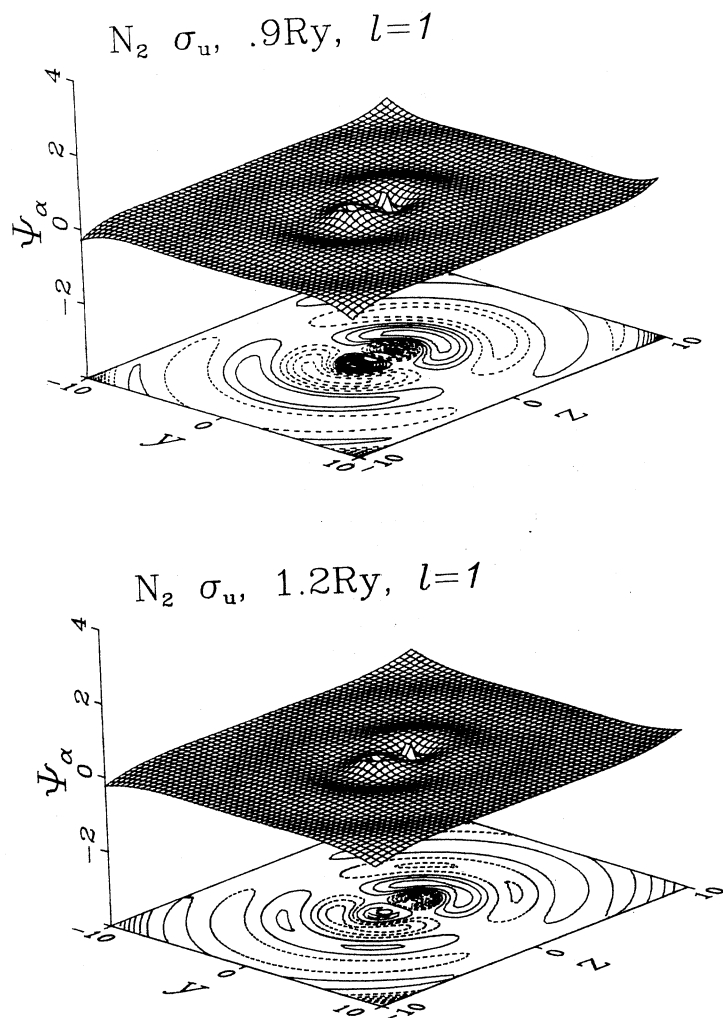


Fig. 6. p-wave-dominated eigenchannel wavefunctions for two electron kinetic energies in the  $\sigma_u$  continuum of  $N_2$ . The molecule is in the  $yz$  plane, along the  $z$  axis, centered at  $y = z = 0$ . Contours mark steps of 0.03, from 0.02 to 0.29; positive = solid, negative = dashed.

tum is not universal and that the angular pattern can be expected, in general, to be more complex. The cusps in the surface mark the nuclear positions. The only apparent change from one surface to the other is the slight shortening of wavelength as the kinetic energy increases. This smooth contraction of nodes continues monotonically through the resonance energy to higher energies. We conclude from Fig. 6 that the  $p$  eigenchannel is indeed nonresonant.

The  $f$ -like eigenchannel, plotted in Fig. 7, exhibits strikingly different behavior. In this case the surfaces (the contours of which have, at large distances, the three nodal planes characteristic of  $f$  orbitals) clearly show the resonant nature of the  $f$  eigenchannel. Note again the definite emergence of a single ( $\ell = 3$ ) orbital momentum character over the whole wavefunction. Below and above (not shown) the resonance energy, the probability amplitude is similar to the  $p$ -wave amplitude. But, at the resonance energy, there is an enormous enhancement of the wavefunction in the molecular interior; the wavefunction now resembles a molecular bound-state probability amplitude distribution. It is this enhancement, in the region occupied by the bound states, that leads to the very large increase in oscillator strength indicative of the resonance, and to the other manifestations discussed earlier and in the next section.

These eigenchannel plots are discussed more fully elsewhere [107]; however, several points should be noted before leaving the subject. First, the  $N_2$  example that we have chosen is somewhat special in that there is a near one-to-one correspondence between the eigenchannels and single values of orbital angular momentum. Orbital angular momentum is, however, not a "good" quantum number in molecules and, generally, we should not always expect such clear nodal patterns. More typically, earlier work [67,96,113,114] indicates that several angular momenta often contribute to the continuum eigenchannels (although a barrier in only one  $\ell$  component will be primarily responsible for the temporary trapping that causes the enhancement in that component, and in components coupled to it), thus implying that the resulting eigenchannel plots will be correspondingly richer. Second, Eqs. (1) and (5) are asymptotic expressions. The orbital momentum composition of these wavefunctions is more complicated in the molecular interior, as seen, for example, in Figs. 6 and 7. Nonetheless, continuity, and a dominant  $\ell$  component may, as in the case of  $N_2$ , cause the emergence of a distinct  $\ell$  pattern, even into the core region. Third, even though these ideas were developed [107] in the context of molecular photoionization, the continuum eigenchannel concept carries over without any fundamental change to electron-molecule scattering. This is a further example of the close connections [68] between shape resonances in molecular photoionization and electron-

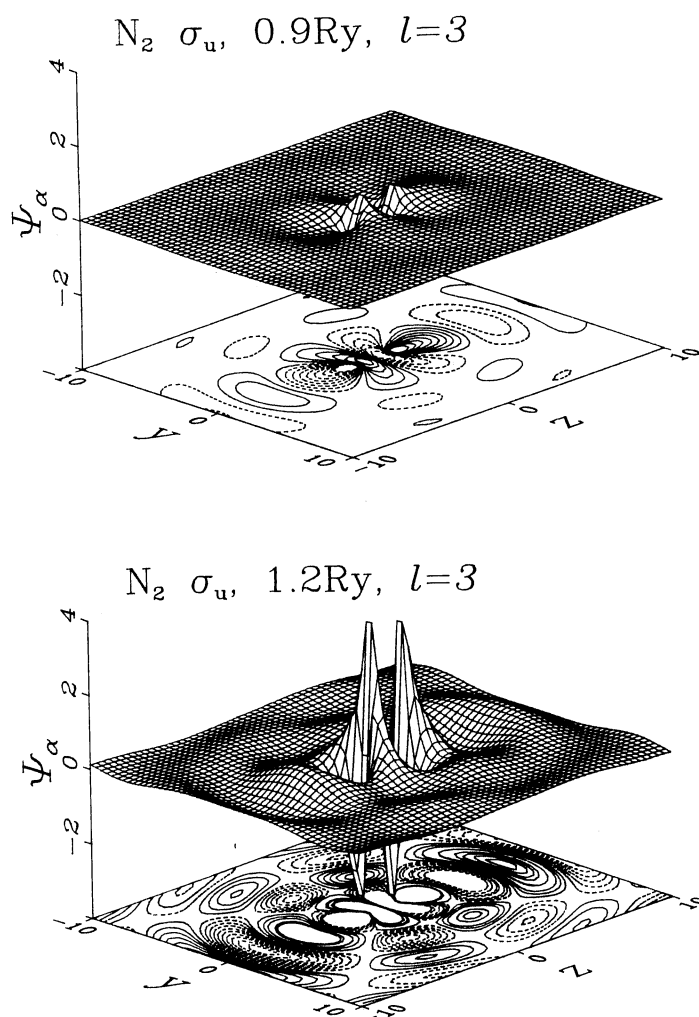


Fig. 7.  $f$ -wave-dominated eigenchannel wavefunctions for nonresonant (top) and resonant (bottom) electron kinetic energies in the  $\sigma_u$  continuum of  $N_2$ . The molecule is in the  $yz$  plane, along the  $z$  axis, centered at  $y = z = 0$ . Contours mark steps of 0.03, from 0.02 to 0.29; positive = solid, negative = dashed. The lack of contour lines near the nuclei for 1.2 Ry is because of the 0.29 cutoff.

molecule scattering. Finally, while we have used one-electron wavefunctions here, obtained within the multiple-scattering model, we emphasize that the eigenchannel concept is a general one, and we look forward to its use in the analysis of more sophisticated, many-electron molecular continuum wavefunctions.

## 2.3 Shape-Resonance-Induced Non-Franck-Condon Effects

### 2.3a Theoretical Predictions

Molecular photoionization at wavelengths unaffected by autoionization, predissociation or ionic thresholds has been generally believed to produce Franck-Condon (FC) vibrational intensity distributions within the final ionic state, and  $v$ -independent photoelectron angular distributions. We now discuss a recent prediction [69,81] that shape resonances represent an important class of exceptions to this picture. These ideas are illustrated with a calculation of the  $3\sigma_g \rightarrow \epsilon\sigma_u$ ,  $\epsilon\pi_u$  photoionization channel of  $N_2$ , which accesses the same  $\sigma_u$  shape resonance as that discussed above, at approximately  $h\nu = 30$  eV, or  $\sim 14$  eV above the  $3\sigma_g$  IP. The potential energy curves for  $N_2$  are shown in Fig. 8 in order to orient this discussion and for later reference in Sections 3 and 4. The process we are considering involves photoexcitation of  $N_2$   $X^1\Sigma_g^+$ , in its vibrational ground state, with photon energies starting from the first IP and extending beyond the region of the shape resonance at  $h\nu \approx 30$  eV. This process ejects photoelectrons, leaving behind  $N_2^+$  ions in energetically accessible states. Fig. 9 shows a typical photoelectron spectrum, measured at  $h\nu = 21.2$  eV, which exhibits photoelectron peaks corresponding to production of  $N_2^+$  in its X, A and B states (i.e., the three lowest ionic states in Fig. 8). Since we are interested in ionization of the  $3\sigma_g$  electron, an event which produces the  $X^2\Sigma_g^+$  ground state of  $N_2^+$ , we are concerned with the photoelectron band in the range  $15.5 \text{ eV} \leq \text{IP} \leq 16.5 \text{ eV}$  in Fig. 9. The physical effects we seek involve the relative intensities and angular distributions of the  $v = 0-2$  vibrational peaks in the  $X^2\Sigma_g^+$  electronic band and, more specifically, the departures of these observables from behavior predicted by the FC separation.

The breakdown of the FC principle arises from the quasibound nature of the shape resonance which, as we discussed in Section 2.2, is localized in a spatial region of molecular dimensions by a centrifugal barrier. This barrier and, hence, the energy and lifetime (width) of the resonance are sensitive functions of internuclear separation  $R$  and vary significantly over a range of  $R$  corresponding to the ground-state vibrational motion. This is illustrated in the upper portion of Figs. 10 and 11, where the dashed curves represent separate, fixed- $R$  calculations of the

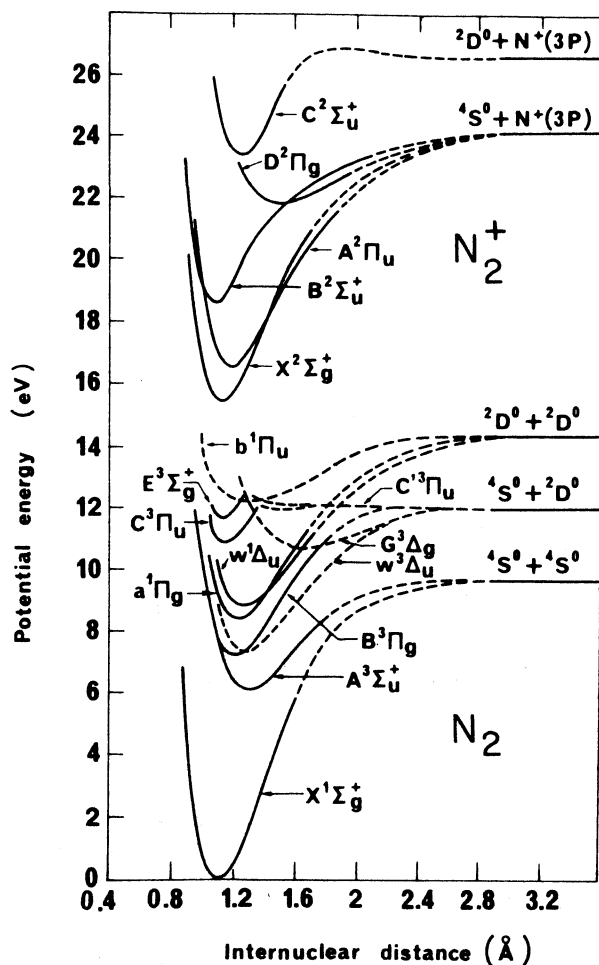


Fig. 8. Potential energy curves for  $N_2$  and  $N_2^+$ .

partial cross-section and asymmetry parameter (respectively) for  $N_2$   $3\sigma_g$  photoionization over the range  $1.824a_0 \leq R \leq 2.324a_0$ , which spans the  $N_2$  ground-state vibrational wavefunction.

Of central importance in Fig. 10 is the clear demonstration that resonance positions, strengths and widths are sensitive functions of  $R$ . In particular, for larger separations, the inner well of the effective potential acting on the  $\ell = 3$  component of the  $\sigma_u$  wavefunction is more attractive, and the shape resonance shifts to lower kinetic energy, becoming narrower and higher. Conversely, for lower values of  $R$ , the resonance is

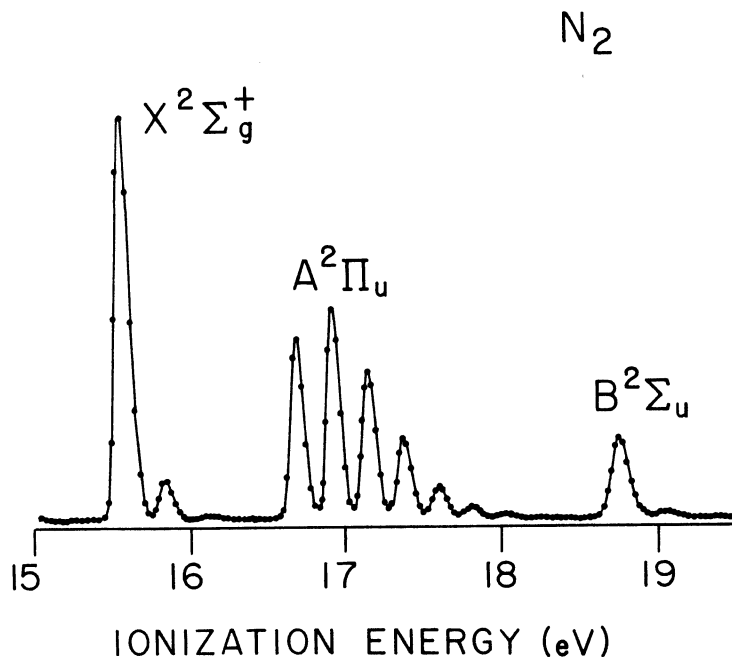


Fig. 9. Photoelectron spectrum of  $N_2$  at  $h\nu = 21.2$  eV.

pushed to higher kinetic energy and is weakened. This indicates that nuclear motion exercises great leverage on the spectral behavior of shape resonances and that small variations in  $R$  can significantly shift the delicate balance between attractive (mainly Coulomb) and repulsive (mainly centrifugal) forces which combine to form the barrier. In the present case, variations in  $R$ , corresponding to the ground-state variation in  $N_2$ , produce significant shifts of the resonant behavior over a spectral range several times the fullwidth at half maximum of the resonance calculated at  $R = R_e$ . By contrast, nonresonant channels are relatively insensitive to such variation in  $R$ , as was shown by results [98] on the  $1\pi_u$  and  $2\sigma_u$  photoionization channels in

Thus, in the vicinity of a shape resonance, the electronic transition moment varies rapidly with  $R$ . This parametric coupling was estimated [69,205], in the adiabatic-nuclei approximation, by computing the net transition moment for a particular vibrational channel as an average of the  $R$ -dependent dipole amplitude, weighted by the product of the initial- and final-state vibrational wavefunctions at each  $R$ :

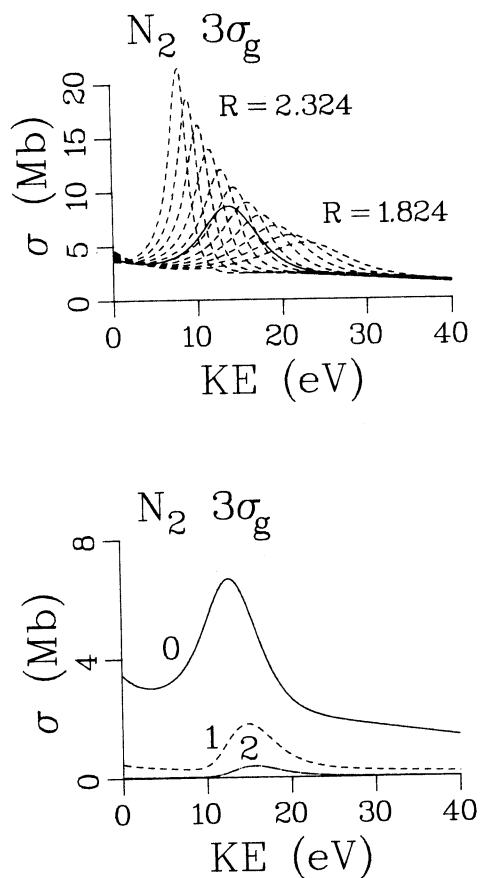


Fig. 10. Cross-sections,  $\sigma$ , for photoionization of the  $3\sigma_g$  ( $v_i = 0$ ) level of  $N_2$ . Top: fixed-R (dashed curves) and R-averaged, vibrationally-unresolved (solid curve) results. Bottom: results for resolved, final-state vibrational levels,  $v_f = 0-2$ .

$$D_{v_f v_i} = \int dR \chi_{v_f}^\dagger(R) D^-(R) \chi_{v_i}(R) . \quad (8)$$

The vibrational wavefunctions were approximated by harmonic-oscillator functions and the superscript " - " denotes that incoming-wave boundary conditions have been applied and that the transition moment is complex. Note that even when the final vibrational levels  $v_f$  of the ion are unresolved (summed over), vibrational motion within the initial state  $v_i = 0$  can cause the

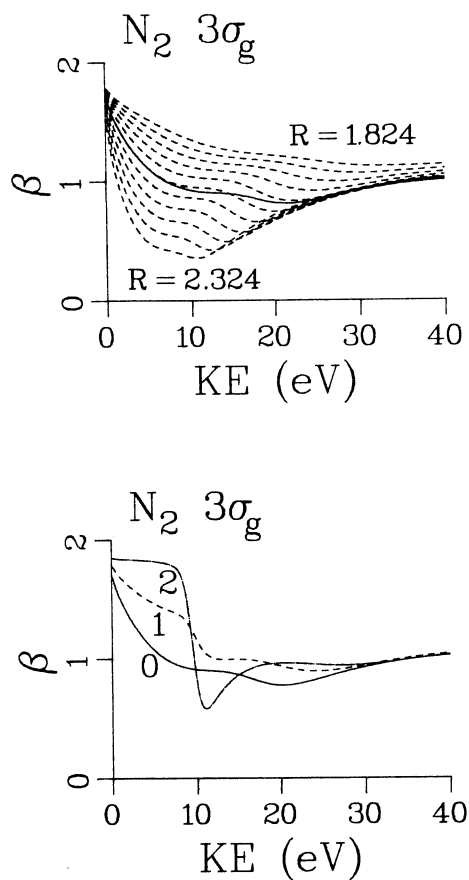


Fig. 11. Asymmetry parameters,  $\beta$ , for photoionization of the  $3\sigma_g$  ( $v_i = 0$ ) level of  $N_2$ . Top: fixed- $R$  (dashed curves) and  $R$ -averaged, vibrationally-unresolved (solid curve) results. Bottom: results for resolved, final-state vibrational levels,  $v_f = 0-2$ .

above equation to yield results significantly different from the  $R = R_e$  result, since the  $R$  dependence of the shape resonance is highly asymmetric. This gross effect of  $R$  averaging can be seen in the upper half of Fig. 10, by comparing the solid line ( $R$ -averaged result, summed over  $v_f$ ) and the middle dashed line ( $R = R_e$ ). Hence, even for the calculation of gross properties of the whole, unresolved electron band, it is necessary to take into account vibrational motion effects in channels exhibiting shape resonances. As we stated earlier, this is generally not a

critical issue in nonresonant channels.

Effects of nuclear motion on individual vibrational levels are shown in the bottom half of Figs. 10 and 11. Looking first at the partial cross-sections in Fig. 10, we see that the resonance position varies over a few volts depending on the final vibrational state and that higher levels are relatively more enhanced at their resonance position than is  $v_f = 0$ . This sensitivity to  $v_f$  arises because transitions to alternative final vibrational states preferentially sample different regions of  $R$ . In particular,  $v_f = 1, 2$  sample successively smaller  $R$ , governed by the maximum overlap with the ground vibrational state, which causes the resonance in those vibrational channels to peak at higher energy than that for  $v_f = 0$ . The impact of these effects on branching ratios is clearly seen in Fig. 12, where the ratio of the higher  $v_f$  intensities to the intensity of  $v_f = 0$  is plotted in the resonance region. There we see that the ratios are slightly above the FC factors (9.3%,  $v_f = 1$ ; 0.6%,  $v_f = 2$ ) at zero kinetic energy, go through a minimum just below the resonance energy in  $v_f = 0$ , then increase to a maximum as individual  $v_f > 0$  vibrational intensities peak and, finally, approach the FC factors again at high kinetic energy. Note that the maximum enhancement over the FC factors is progressively more pronounced for higher  $v_f$ , i.e., 340% and 1300% for  $v_f = 1, 2$ , respectively.

The effects on  $\beta(v_f)$ , shown in the lower portion of Fig. 11, are equally dramatic. Especially at and below the resonance position, the  $\beta$ 's vary greatly for different final

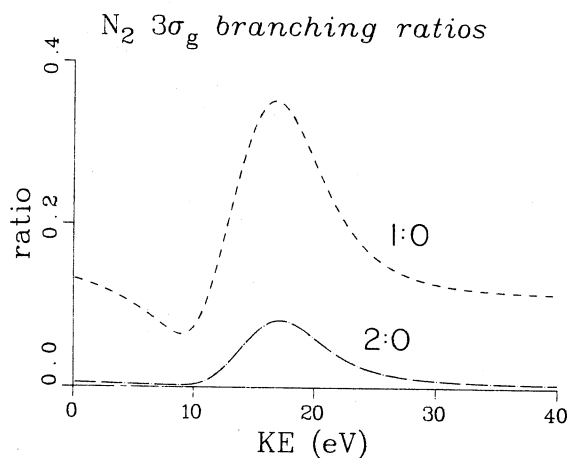


Fig. 12. Vibrational branching ratios  $\sigma(v_f)/\sigma(v_f=0)$  for photoionization of the  $3\sigma_g$  level of  $N_2$ .

vibrational levels. The  $v_f = 0$  curve agrees well with the solid curve (in the upper half) since the gross behavior of the vibrationally-unresolved electronic band will be governed by the  $\beta$  of the most intense component. The  $R = R_e$  curve has been found to agree well with recent wavelength-dependent measurements [75,78] and the agreement is improved by the slight damping caused by  $R$  averaging. More significant for the present discussion, however, is the  $v_f$  dependence of  $\beta$ . Carlson first observed [175,184] that, at 584 Å, the  $v_f = 1$  level in the  $3\sigma_g$  channel of  $N_2$  had a much larger  $\beta$  than the  $v_f = 0$  level, even though there was no apparent autoionizing state at this wavelength. This is in semiquantitative agreement with the present calculation which gives  $\beta(v_f = 0) \approx 1.0$  and  $\beta(v_f = 1) \approx 1.5$ . Although the agreement is not exact, we feel this demonstrates that the "anomalous"  $v_f$  dependence of  $\beta$  in  $N_2$  stems mainly from the  $\sigma_u$  shape resonance, a resonance which acts over a range of the spectrum many times its own  $\sim 5$  eV width. The underlying cause of this effect is the shape-resonance-enhanced  $R$  dependence of the dipole amplitude, just as for the vibrational partial cross-sections. In the case of  $\beta(v_f)$ , however, both the  $R$  dependence of the phase and of the magnitude of the complex dipole amplitude play a crucial role, whereas the partial cross-sections depend only upon the magnitude.

The above prototypical study demonstrates several new aspects of photoionization channels exhibiting shape resonances: First, the time delay in photoelectron escape, associated with a shape resonance, enhances the coupling between nuclear motion and electronic motion, invalidating the FC factorization of the two modes. In time-independent language, the great asymmetric and nonmonotonic sensitivity of the transition amplitude to internuclear separation requires a folding of the transition amplitude with the vibrational motion of the molecule, at the very least in an adiabatic scheme. When resonance lifetimes and the vibrational period are comparable, nonadiabatic effects (analogous to those observed [195,196] for the 2.4 eV  $\pi_g$  resonance in  $e-N_2$  scattering) are likely to be important as well. Second, shape resonance effects are large for both vibrational intensities and angular distributions, but were largely overlooked in earlier work because these effects tend to lie in an inconvenient wavelength range for laboratory light sources. Synchrotron radiation has since solved this problem, as discussed in the next section. Third, it is significant to note that the effects of the shape resonance, as described above, act over tens of volts of the spectrum, several times the half-width of the resonance, and that  $\sigma$  and  $\beta$  probe the effects differently, i.e.,  $\sigma$  and  $\beta$  exhibit maximal effects in different energy regions. This underscores the well-known difference in dynamical information contained in the two physical observables. Fourth, a long-standing "anomalous"  $v_f$  dependence in the photoelectron angular

distributions of the  $3\sigma_g$  channel of  $N_2$  has been resolved. Finally, the phenomena described here for one channel of  $N_2$  should be very widespread since shape resonances now appear to affect one or more inner- and outer-shell channels in most small (non-hydride) molecules.

### 2.3b Triply-Differential Photoelectron Measurements

In order to fully examine dynamical aspects discussed in earlier sections, especially the last section, it is essential to perform measurements of photoelectron intensity as a function of three independent variables --- wavelength of the incident light, to select the spectral features; photoelectron kinetic energy, to select the ionization channel of interest; and ejection angle, to measure angular distributions. For convenience, we refer to this level of experiment as "triply-differential" photoionization experiments. Over the last few years, electron spectroscopy has been combined with synchrotron radiation sources to achieve successful triply-differential measurements in molecules, including vibrational state resolution. Presently several groups (e.g., [75,157-163]) in the U.S., France, Germany and England are involved in this type of experiment, each with its own specific experimental configuration and special emphasis, but each fulfilling the requirements for full triply-differential studies. Here we will review, as an example, the experimental aspects of a new instrument [163] at the Synchrotron Ultraviolet Radiation Facility (SURF-II), at the U.S. National Bureau of Standards, in order to focus on some of the experimental considerations in triply-differential photoionization studies. After a review of experimental techniques, we show how earlier measurements at SURF-II [99] and elsewhere [79] were used to test the predictions of non-FC effects in  $N_2$  photoionization.

The new triply-differential electron spectrometer system at NBS consists of a high-throughput, normal-incidence monochromator [206] (Fig. 13) and a pair of 10 cm mean-radius hemispherical electron spectrometers in an experimental chamber (Fig. 14). To avoid later confusion, we note that an earlier configuration using the same monochromator with a single, rotatable 5 cm mean-radius spectrometer [159] has been used for the past five years in several triply-differential photoionization studies and is, in fact, the instrument used to obtain the data presented later in Figs. 15, 27 and 28. The special emphasis with both generations of instruments has been the same, namely, to optimize the photon and electron resolution in order to probe detailed dynamics within shape resonance and autoionization structure in the near-normal-incidence range ( $h\nu \leq 35$  eV). The new instrument further optimizes several aspects of the electron spectrometer system to greatly extend the sensitivity and/or resolution com-

# HIGH THROUGHPUT NORMAL INCIDENCE MONOCHROMATOR AT SURF-II

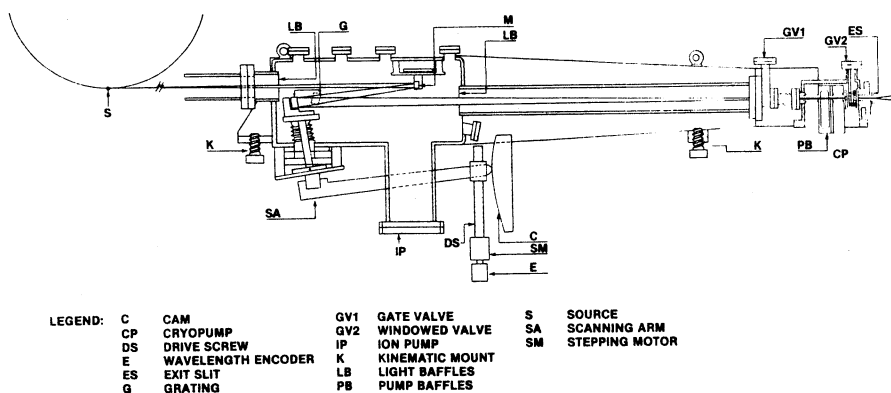


Fig. 13. Schematic diagram of high-throughput, normal-incidence monochromator (taken from [206]).

pared to earlier measurements, for reasons discussed in Section 3.

The high-flux, 2-meter monochromator shown in Fig. 13 has been specifically matched to the characteristics of the SURF-II storage ring: First and foremost, it uses the small vertical dimension of the stored electron beam ( $\sim 80 \mu\text{m}$ ) as the entrance aperture of the monochromator, a unique feature which eliminates loss of incident flux on the entrance slit. Second, it is attached directly to the exit port of the storage ring, resulting in a very large capture angle of 65 mrad in the horizontal plane. This arrangement produces approximately  $10^{10}$  photons  $\text{sec}^{-1}\text{\AA}^{-1}$  per mA of circulating current (typical initial current  $\approx 15$  mA) at  $1000 \text{\AA}$  and has been used for triply-differential measurements down to  $\sim 375 \text{\AA}$ . Together with a 1200 line/mm grating and a  $200 \mu\text{m}$  ( $100 \mu\text{m}$ ) exit slit, this configuration yields a photon resolution of  $\sim 0.8 \text{\AA}$  ( $0.4 \text{\AA}$ ). Plans have been made to improve the resolution with a higher-dispersion grating. The dispersed light is channeled by a 2 mm i.d. capillary tube for a distance of  $\sim 25$  cm into the interaction region of the experimental chamber. The low pumping conductance of this capillary tube is very effective in reducing the gas load on the monochromator and storage ring during experiments in which the gas pressure in the experimental chamber can be as high as  $10^{-4}$  torr.

The new electron spectrometer system is shown schematically

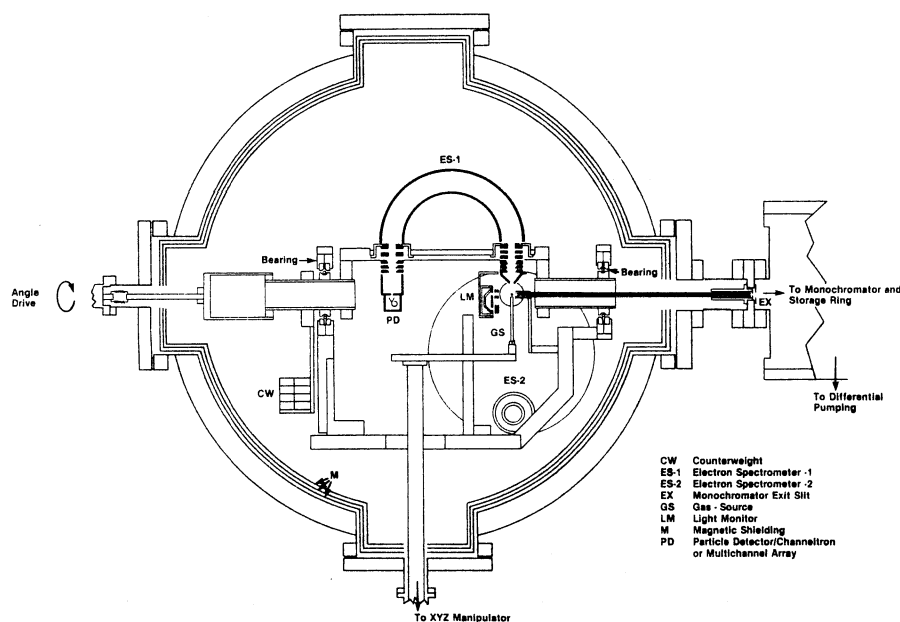


Fig. 14. Schematic diagram of dual electron spectrometer system (taken from [163]).

in Fig. 14. The chamber is a 76 cm diameter, 92 cm long stainless-steel vacuum chamber. It is pumped by a 500 liter/sec turbomolecular pump and a 2000 liter/sec closed-cycle helium cryopump to provide maximum flexibility in studying the whole range of gaseous targets. Low magnetic fields of  $<500 \mu\text{gauss}$  are maintained throughout the chamber by three layers of high-permeability magnetic shielding.

The system is designed to operate with either one rotating (ES-1) or two (ES-1 and ES-2) electron spectrometers. In either configuration the electron spectra can be recorded as a function of ejection angle relative to the principle axis of polarization. This leads to the determination of the photoelectron branching ratios and angular distributions according to the following expression, which applies to dipole excitation of free molecules with elliptically-polarized light [159,207]:

$$\frac{d\sigma_V}{d\Omega} = \frac{\sigma_V}{4\pi} \left[ 1 + \frac{\beta_V}{4} (3P \cos 2\theta + 1) \right] \quad (9)$$

where,

- $\beta_v$  = asymmetry parameter for vibrational state v.
- $\sigma_v$  = total cross-section for transition to vibrational state v.
- P = polarization of the light with the horizontal component being the major axis.
- $\theta$  = angle of ejection of photoelectrons with respect to the horizontal direction.

The number of electrons ejected per unit light flux per unit solid angle,  $dn_v/d\Omega$ , is proportional to the differential cross-section and, hence, we can write:

$$\frac{dn_v}{d\Omega} = N_v \left[ 1 + \frac{\beta_v}{4} (3P \cos 2\theta + 1) \right]. \quad (10)$$

Measurement of P,  $\theta$  and the number of electrons as a function of  $\theta$  enables a determination of  $\beta_v$  and  $N_v$ .  $N_v$ , when normalized over a relevant set of possible alternative ionization channels, gives the branching ratio for the particular transition. The measurement of P is accomplished with a triple-reflection polarizer based upon the considerations of Horton, *et al.* [208]. The incoming light flux is monitored by a 90% transparent tungsten photocathode on the input aperture of the polarization monitor. After three reflections, the light is intercepted by a second tungsten photodiode. The ratio of these two photodiode signals, at  $0^\circ$  and  $90^\circ$  with respect to the major polarization axis, determines the polarization.

Each electron analyzer is a 10 cm mean-radius version of our previous instrument [159] and maintains the same electron-lens system --- a three-aperture zoom lens to focus the electrons into the hemispherical dispersive element and a similar one to refocus the energy-analyzed electrons on the exit slit. There are no entrance or exit apertures in the equatorial plane of the hemisphere and, therefore, the aperture in the entrance cone determines the basic resolution. This entrance aperture, and an aperture in front of the channeltron, are changeable to ensure control of geometric constraints on the resolution. The resolution obtainable, while yet maintaining a good signal, is expected to be on the order of 20 meV. This resolution is a significant improvement over that typically used now and will allow for the extension of studies of non-Franck-Condon effects to small polyatomic molecules.

The electrical aspects of the electron spectrometer are maintained much as in the previously described apparatus [159].

Briefly, the fixed voltages are controlled by highly regulated conventional power supplies and the variable voltages are under computer control. A 16 bit digital-to-analog converter (DAC) with a basic increment of 0.0005 V controls the ramping of off-set voltages. The variable focus voltages are controlled by isolated power sources run by the computer. The computer (LSI-11) resides in a CAMAC crate and also controls the grating drive, angular position, light-detecting system, electron-counting system and other experimental chores. Both analyzers are ramped off the 16 bit DAC but have their own separately controlled power supplies for lens voltages. The two identical instruments will allow a determination of the branching ratios and asymmetry parameters without rotation (i.e., the electron intensity at two angles can be measured simultaneously). The device can be calibrated by reference to a gas with a known cross-section [209] and asymmetry parameter [192,210]. The calibration features for the two instruments are incorporated into a computer program that analyzes and reduces the data. Area detectors have been purchased and will soon be integrated into the experiment, thus significantly increasing the sensitivity of the system.

The gas-inlet system is mounted on an XYZ manipulator for external alignment of the gas jet to optimize signal intensity and resolution. Exit nozzles of the system are interchangeable and provide both effusive beams and supersonic jets by use of pinhole apertures of diameter 7-50  $\mu\text{m}$ . The positioning of the supersonic source is of particular importance and necessitates the positioning capability of this inlet system. With the larger hemispherical dispersive element, the use of two analyzers, better gas-source technology, incorporation of area detectors and enhanced pumping, we expect a significant improvement in basic sensitivity of the instrument (a very conservative estimate would be >100x) as compared to our present 5 cm radius single-analyzer system.

The same LSI-11 computer used for automation is also used for data reduction. The basic data consist of electron counts as a function of wavelength, ramp voltage and angle. The ramp voltage is converted, using known quantities, to electron kinetic energy. The electron counts are then normalized for correction factors that depend upon kinetic energy, such as the transmission functions of the instruments and any angular correction factors. Upon obtaining a suitably normalized set of data, the photoelectron spectra are fitted to a gaussian basis set, using spectroscopic values for vibrational energy spacings, and treating peak height, peak width and overall position as free parameters. The areas of the respective peaks are used to infer the values of the branching ratios and asymmetry parameters from the equation given above. The calculated curve and normalized data

are plotted to aid in the evaluation of the quality of fit. In addition, this fitting program outputs statistical parameters which can be used to estimate accuracy.

### 2.3c Experimental Confirmation of Non-FC Effects

The theoretical predictions of Section 2.3a were soon tested in two separate experiments, as indicated in Figs. 15 and 16. In Fig. 15, the branching ratio for production of the  $v=0$  and 1 vibrational levels of  $N_2^+ X \ 2\Sigma_g^+$  is shown. The dash-dot line is the original prediction [69] from Fig. 12. The solid dots are recent measurements [99] in the vicinity of the shape resonance at  $h\nu \approx 30$  eV. The conclusion drawn from this comparison is that the observed variation of the vibrational branching ratio relative to the FC factor over a broad spectral range qualitatively confirms the prediction; however, subsequent calculations [94,109] with fewer approximations have achieved much better

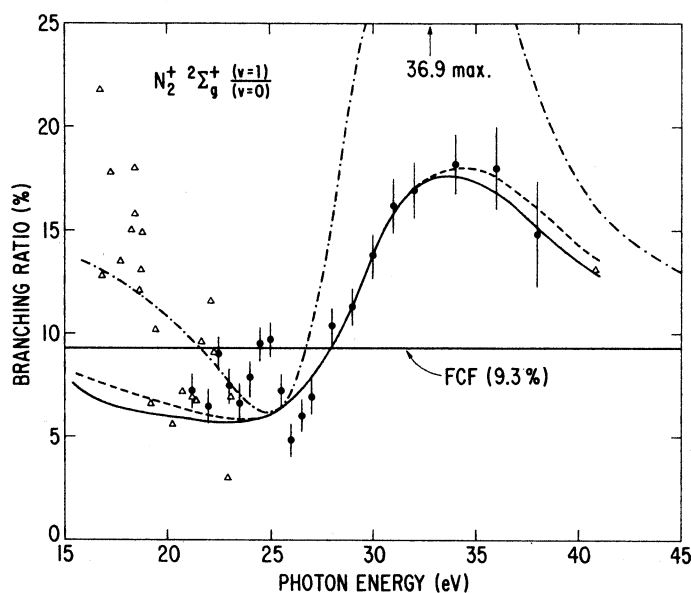


Fig. 15. Branching ratios for production of the  $v = 0, 1$  levels of  $N_2^+ X \ 2\Sigma_g^+$  by photoionization of  $N_2$ . References: ●, [99]; Δ, [181]; ---·---, multiple-scattering model prediction from [69]; —, frozen-core Hartree-Fock dipole-length approximation from [109]; ---, frozen-core Hartree-Fock dipole-velocity approximation from [109].

agreement based on the same mechanism for breakdown of the FC separation. The dashed and solid curves in Fig. 15 are results based on a Schwinger variational treatment [109] of the photoelectron wavefunction. The two curves represent a length and velocity representation of the transition matrix element, both of which are in excellent agreement with the data. This is an outstanding example of interaction between experiment and theory, proceeding as it did from a novel prediction, through experimental testing, and final quantitative theoretical agreement in a short time. Also shown in Fig. 15 are data in the  $15.5 \text{ eV} \leq h\nu \leq 22 \text{ eV}$  region which represent earlier results [181] obtained using laboratory line sources. The apparently chaotic behavior arises from unresolved autoionization structure, the detailed study of which is discussed in Section 3.3.

Fig. 16 shows angular distribution asymmetry parameters,  $\beta$ , for the  $v=0,1$  levels of  $\text{N}_2^+ \text{X}^2\Sigma_g^+$  over roughly the same energy region as that discussed above. These data were obtained at the Synchrotron Radiation Center at the University of Wisconsin by Carlson and co-workers [79]. In the region above  $h\nu \approx 25 \text{ eV}$ , these data also show qualitative agreement with the predicted [69]  $v$  dependence of  $\beta$  caused by the  $\sigma_u$  shape resonance. In this case, the agreement is somewhat improved in later calcula-

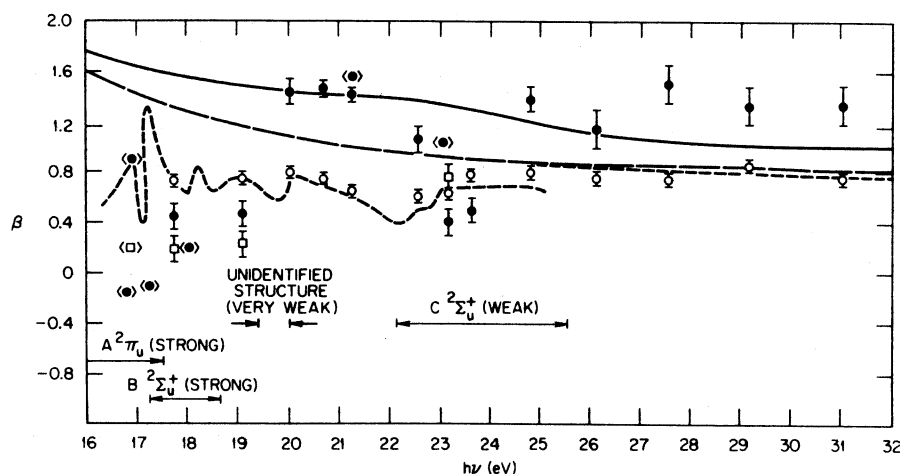


Fig. 16. Photoelectron asymmetry parameters for the  $v = 0,1$  levels of  $\text{N}_2^+ \text{X}^2\Sigma_g^+$ . References: o,  $v = 0$  data from [79]; •,  $v = 1$  data from [79]; long-dashed curve,  $v = 0$  prediction from [69]; solid curve,  $v = 1$  prediction from [69]; other data described in [79], from which this figure was taken.

tions [109], mainly for  $v=1$ ; however, the change is less dramatic than for the branching ratios.

## 2.4 Progress and Prospects

In summary, we have used prototypical studies on  $N_2$  to convey the progress made in the study of shape resonances in molecular photoionization, most of which has occurred over the last ten years or so. This included the identification of shape-resonant features in photoionization spectra of molecules and the accrual of substantial physical insight into their properties, many of which are peculiar to molecular fields. One very recent example has been the prediction and experimental confirmation of the role of shape resonances in producing non-Franck-Condon effects in vibrational branching ratios and photoelectron angular distributions.

What this discussion has failed to convey so far is the already extensive body of work that has developed around these basic themes. Even in an early interpretation [20] of shape resonance effects in x-ray spectra, it was obvious that the phenomena would be widespread since more than ten molecules, or local molecular moieties, were observed (see, e.g., [8,20]) to exhibit shape-resonant behavior. At the present, it is not difficult to identify over two dozen examples of molecules exhibiting the effects discussed above, in one or more final-state symmetries. (The following examples are found in [2-134] and the inner-shell cases are listed according to molecule in the bibliography given by Hitchcock [3].) These include simple diatomics ( $N_2$ ,  $O_2$ , CO, NO), polyatomics with subgroups related to the first-row diatomics (HCN,  $C_2N_2$ ,  $CH_3CN$ ), triatomics ( $CO_2$ ,  $CS_2$ , OCS,  $N_2O$ ,  $SO_2$ ) and more highly coordinated molecules and local molecular environments ( $SF_6$ ,  $SO_4^{2-}$ ,  $SF_5CF_3$ ,  $SF_2O_2$ ,  $SF_2O$ ,  $BF_3$ ,  $SiF_4$ ,  $SiCl_4$ ,  $SiF_6^{2-}$ ,  $SiO_2$ ,  $NF_3$ ,  $CF_4$ ). There is no doubt that many cases have been overlooked in this listing and that many more examples will be identified in the future as the exploration of molecular photoionization dynamics continues, particularly with the increasing utilization of synchrotron radiation sources.

Several examples from the above body of literature serve both to emphasize some of the interesting complications that can arise, and to caution against assuming that manifestations of shape resonances will always conform to the independent-electron concepts used above to explain the fundamentals of the subject in connection with  $N_2$  photoionization: (i) For example, in the iso-electronic molecule CO, much of what was said for  $N_2$  would carry over with suitable modifications to account for the loss of inversion symmetry. However, for photoionization of the outermost  $5\sigma$  orbital (the counterpart of the  $3\sigma_g$  in  $N_2$ ) the vibrational branching ratios [76] and  $\beta$ 's [80] *for the weaker*  $v \geq 2$

*channels* deviate qualitatively from calculations [112]. This has been postulated [112] to arise from channel interaction with weak, doubly-excited autoionizing states in the region of the shape resonance. In any case, some departures from the simplified picture drastically alter the otherwise anticipated behavior of these weak vibrational channels. (ii) In the case of  $O_2$  photoionization, an analogous  $\sigma_u$  shape resonance is expected [84,111,119] but its identification in the photoionization spectrum has been complicated by the existence of extensive autoionization structure in the region of interest. Recent work [132], using variable-wavelength photoelectron measurements and an MQDT analysis of the principal autoionizing Rydberg series, has sorted out this puzzle, with the result that the  $\sigma_u$  shape resonance was established to be approximately where expected but was not at all clearly identifiable without extensive analysis. (iii) In the case of  $CO_2$ , a  $\sigma_u$  shape resonance of completely different origin was expected [85,96] in photoionization of the  $4\sigma_g$  orbital, leading to the  $C\ 2\Sigma_g^+$  state of  $CO_2^+$ . This resonance, however, was not apparent in partial cross-section measurements on this channel [56], for reasons still not definitely known. Nevertheless, predictions [85,113] of a shape-resonant feature in the corresponding  $\beta$  were confirmed [101] and results from several laboratories [85,92,96,101,102,108,110,113,122] have now converged to reasonable agreement for this observable. Future experimental work on vibrational branching ratios [113] and v-dependent  $\beta$ 's [113] would greatly aid in the further study of this puzzle. (iv) The most dramatic display of shape resonance phenomena is in  $SF_6$ , a molecule which exhibits four prominently-enhanced features ( $a_{1g}$ ,  $t_{1u}$ ,  $t_{2g}$  and  $e_g$  symmetries) in its inner-shell spectrum [4,5,20]. However, the role of the  $t_{2g}$  and  $e_g$  shape resonances in valence-shell spectra is poorly established. The experimental and theoretical evidence is too involved to summarize here; however, we do note that strong evidence [129], associated with the behavior of the  $t_{2g}$  resonance, exists for strong channel interaction among valence-shell photoionization channels. Moreover, the failure to clearly observe [55,74] the  $e_g$  resonance also suggests substantial departures from the elementary ideas described above. (v) Finally, returning to the case of  $N_2$ , we note that the photoionization of the  $2\sigma_g$  should also access the  $\sigma_u$  shape resonance. However, for this inner-valence orbital, extensive vibronic coupling causes a breakdown [211] of the single-particle model, leading to the observation [91] of tens of "satellite" vibronic states in the photoelectron spectrum instead of a single peak due to ionization of the  $2\sigma_g$  orbital. Nevertheless, if the intensity of this complicated structure is summed and plotted versus photon energy, the resonant enhancement reemerges.

These five cases are excellent examples of the additional challenges that can arise in the study of shape resonance phenom-

ena. These challenges should not diminish the simplicity and power of the fundamental shape resonance dynamics; rather, they show how the fundamental framework showcases more complicated (and interesting) photoionization dynamics which, in turn, require a more sophisticated framework for full understanding.

Another form of progress is measured by the applicability of ideas to other observables or, more broadly, to other subfields:

- (i) We have already touched upon the close connection [68] between shape resonance phenomena in molecular photoionization and electron-molecule scattering. The mapping of the set of shape resonances from one case to the other by a shift of  $\sim 10$  eV on the kinetic energy scale has been discussed elsewhere [68].
- (ii) Shape resonances in adsorbed molecules are now used rather extensively [197,198] as a probe of the geometry and electronic properties of adsorption sites.
- (iii) As discussed in connection with inner-shell spectra of  $\text{SF}_6$ , free-molecule concepts concerning localized states carry over to the condensed phase. In such cases a local "molecular" point of view can often provide more direct physical insight into photoexcitation dynamics of solids than does a band-structure approach. It is interesting to note that shape-resonant features in solid  $\text{SiO}_2$ , interpreted [20] long ago, are now used to monitor the oxidation of silicon in the fabrication of metal-oxide semiconductors.
- (iv) As noted above, shape resonances are often low-energy precursors to EXAFS structure occurring from  $\sim 100$  eV to thousands of eV above inner-shell edges. In fact, such resonant features are very sensitive to local structure (cf. Section 2.3) and may be very useful for local structure determination.
- (v) An intimate connection also exists with antibonding valence states in quantum chemical language. This was dramatically demonstrated over ten years ago, when Gianturco, *et al.* [21] interpreted the shape resonances in  $\text{SF}_6$  using unoccupied virtual orbitals in an LCAO-MO calculation. This connection is a natural one since shape resonances are localized within the molecular charge distribution and therefore can be realistically described by a limited basis set suitable for describing the valence MO's. However, the scattering approach used in the shape resonance picture is necessary for analysis of various dynamical aspects of the phenomenon.
- (vi) Finally, shape resonances have been used as characteristic features in the analysis of such diverse subjects as electron optics [67] of molecular fields and hole localization [54] in inner-shell ionization, and as the cause for molecular alignment in photoionization, leading to anisotropy in the angular distributions [82] of Auger electrons from the decay of K-shell holes.

Looking to the future, there are several enticing prospects for significant progress. For instance, the present set of known and characterized resonance features is only the tip of

the iceberg. The joint theoretical and experimental efforts needed to extend our knowledge of these useful states to other molecules and to other detection channels should be very fruitful and should present new issues to be resolved. Another theme, so natural in research, is the study of those cases in which our prevailing ideas break down. Several examples were cited above but this is expected to be a major growth area in molecular photoionization dynamics, owing to the growth both in detailed experimental studies and in the variety of computational methods capable of treating inter- and intra-channel coupling and non-Born-Oppenheimer effects. In this context, the study of weak channels, such as weak vibrational channels, should be most useful in highlighting the departures from the independent-particle, adiabatic framework used above. Another obvious example is the potential for more active investigations of shape-resonantly localized excitations in other contexts, such as adsorbed molecules, solids and biological molecules. In these and unforeseen ways, the expansion, refinement and unification of recent developments in the study of shape resonances in molecular fields will provide a stimulating theme in molecular physics in the coming years.

### 3. MOLECULAR AUTOIONIZATION

#### 3.1 Overview

Autoionization is an intrinsically multichannel process in which an excited discrete state from one channel couples to the underlying electronic continua of one or more other channels to effect ionization. It has been known since Fano's original work [1,212,213], almost fifty years ago, that this process produces characteristic asymmetric Fano-Beutler profiles in the photoionization cross-section. Since then, there have been extensive studies of autoionization structure in photoionization spectra of atoms [1] and molecules (see, e.g., [2,120,214-228]). In addition, the manifestations of autoionization in dynamical parameters such as photoionization branching ratios and photoelectron angular distributions have been recognized and have recently evolved into a major focal point for current studies of molecular photoionization dynamics (see, e.g., [64,93,116,125,132-134, 137-150,164-193,229-230]).

A more physical description of the autoionization process is helpful in discussing the alternative decay mechanisms possible in molecules: In most cases, autoionizing states consist of an excited Rydberg electron bound to an excited ion (also called core), primarily by Coulomb attraction. (The case of two highly correlated electrons bound to an ion is another important example, but one which requires special treatment [231] and

will not be discussed here.) A necessary condition for decay of this state by ionization is that the excitation energy of the ion core be greater than the binding energy of the Rydberg electron. Then, barring alternative decay paths, autoionization will take place by means of a close collision, between the Rydberg electron and the core, in which excitation energy of the core is transferred to the excited electron to overcome its binding energy and to permit its escape from the ionic field. Note that although a Rydberg electron spends only a very small fraction of time within the molecular ion, such close encounters are essential for autoionization, since only when the Rydberg electron is nearby can it participate fully in the dynamics of the core and exchange energy efficiently with it.

A molecular ion core can store the energy needed to ionize a Rydberg electron in any of its three modes -- electronic, vibrational or rotational. The most direct means of storing electronic energy is the production of a hole in a molecular orbital other than the outermost occupied MO by, for example, promoting one of the inner electrons into a Rydberg orbital to initially prepare the autoionizing state. In addition, various degrees of vibrational and rotational excitation can accompany photoexcitation of Rydberg states. It is the existence of, and interplay among, the alternative energy modes which lead to the unique properties of molecular autoionization.

As a concrete example of rotational and vibrational autoionization, we shall discuss photoionization of  $H_2$ . The alternative rovibrational ionization channels for para- $H_2$  ( $J=0$ ) are shown schematically in Fig. 17. The ground ionic state,  $H_2^+ X^2\Sigma_g^+$ , is the only bound electronic state in this spectral range; hence, the possibility of electronic autoionization is eliminated. In Fig. 17, the vertical, shaded bars represent various vibrational channels of  $H_2^+ X^2\Sigma_g^+$ , labeled by  $v^+=0-5$ . Pairs of continua are associated with each  $v^+$ , reflecting the two rotational continua  $N^+=0,2$  produced by photoionization of para- $H_2$ . Converging to each of these (and higher) rovibrational thresholds is a Rydberg series supported by the Coulomb field of the  $H_2^+$  ion. A small subset of these Rydberg states is indicated, for later reference, by horizontal lines at the observed spectral locations, with each state being placed directly under the threshold to which it converges. Any of these optically allowed Rydberg states can autoionize by coupling with accessible open channels. In this case, autoionization would proceed by transferring energy stored in rotation or vibration of the ion core to the photoelectron. If more than one continuum is available, the decay will proceed into each with a branching ratio determined by the detailed dynamics of the decay process. Moreover, the angular distribution of the photoelectrons escaping in

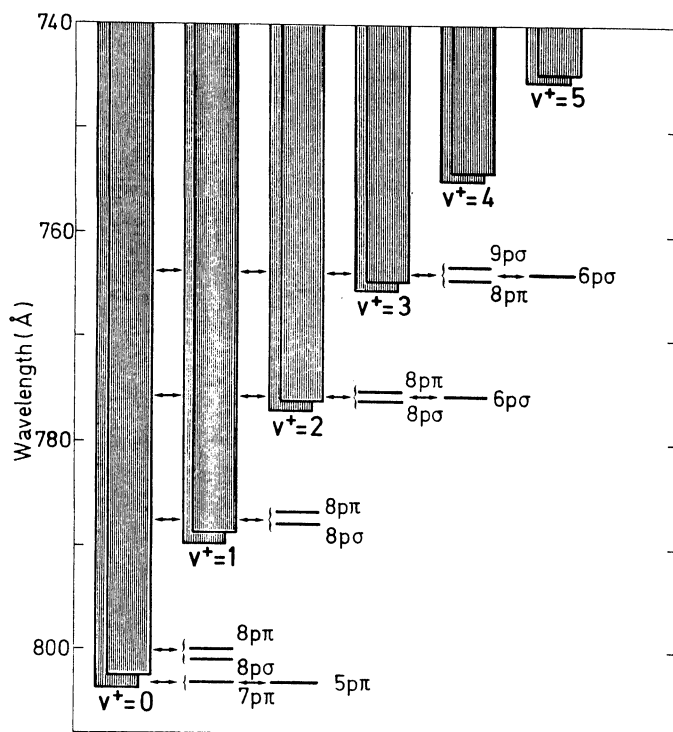


Fig. 17. Schematic illustration of vibrational-rotational autoionization in cold para- $\text{H}_2$  ( $J = 1$ , negative parity final states). Continua are indicated by vertical hatching. For each given  $v^+$  of the ion  $\text{H}_2^+$  there are two continua corresponding to rotational quantum number  $N^+ = 0$  and 2 of the ion ( $J = 1$ ). Selected discrete Rydberg levels are indicated below the vibrational ionization limit with which they are associated (taken from [148]).

each channel will reflect further details of the dynamics, including relative phases of degenerate photoelectron wavefunctions.

Based on the picture, so far, of a set of rovibrational thresholds and Rydberg series converging to each threshold, one might expect a dense pattern of autoionizing levels, but one which would straightforwardly yield to spectroscopic analysis in terms of characteristic rovibrational spacings and the known behavior of Rydberg series. However, this simple picture of a rich, but fundamentally uncomplicated, spectrum ignores all in-

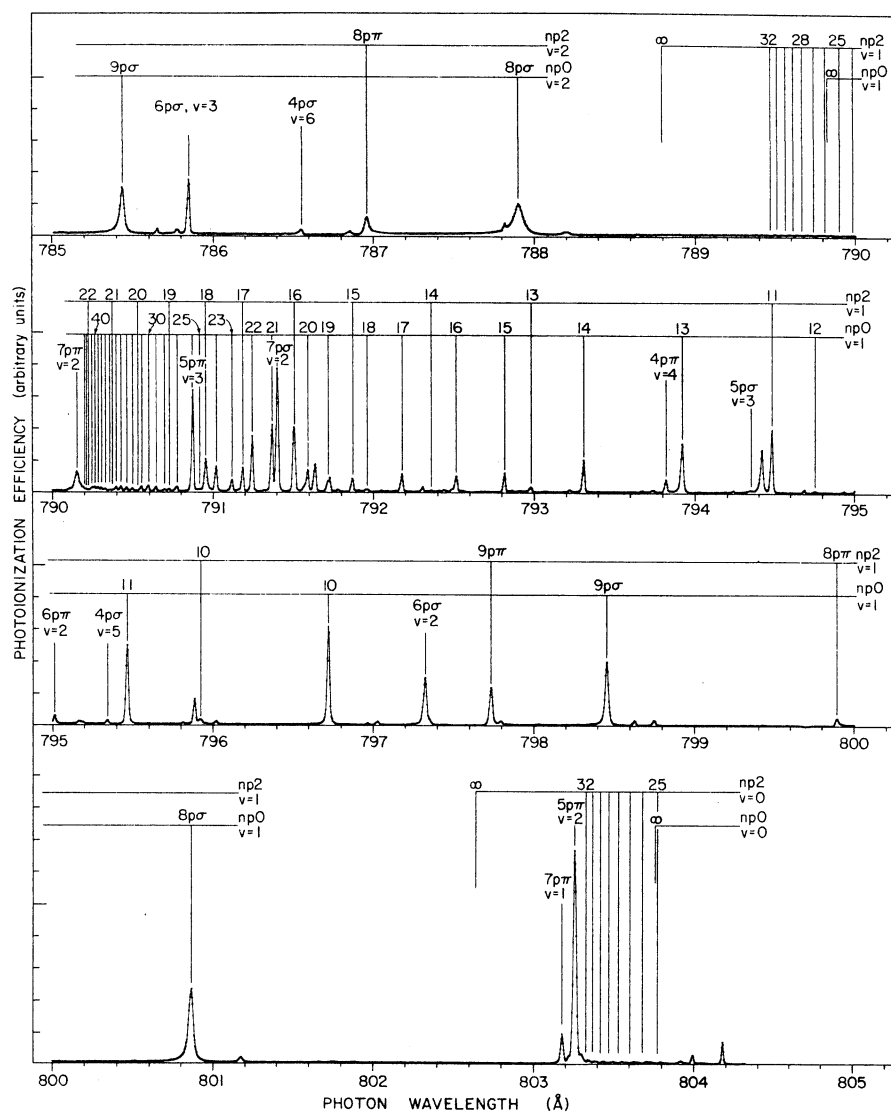


Fig. 18. A portion of the photoionization cross-section of para- $\text{H}_2$  at  $78^\circ\text{K}$  (taken from [220]).

interaction between the Rydberg electron and the molecular core, and is wrong. This is demonstrated dramatically in Figs. 18 and 19, which show the total photoionization spectrum in two spectral regions (chosen for later discussion) covered in Fig.

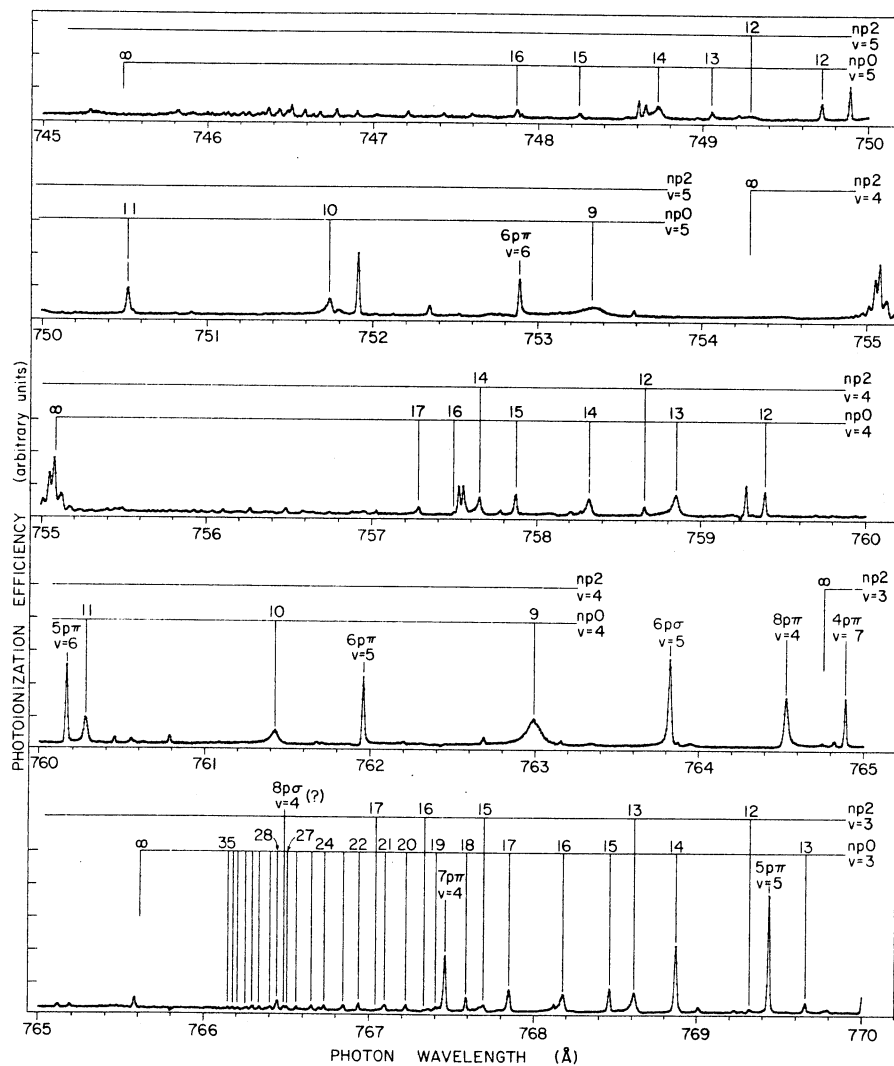


Fig. 19. A portion of the photoionization cross-section of para- $\text{H}_2$  at  $78^\circ\text{K}$  (taken from [220]).

17 --- one region from the first IP to 785 Å and the other from 770-745 Å. Careful inspection reveals that, for any Rydberg series, the spacings, intensities and profiles differ strongly from a simple Rydberg pattern. This is especially true near "interlopers", i.e., Rydberg states falling in the midst of a Rydberg series but converging to a higher limit. For such cases, level shifts and intensity redistribution frequently modify the entire host Rydberg series. These modifications arise from mutual interactions mediated by short-range forces and have been accounted for in detail in this prototypical system.

In the following two sections, we discuss two examples which represent the state-of-the-art in theoretical and experimental studies of molecular autoionization dynamics. The most accurate and penetrating theoretical analysis [137-139,143-145,147,148] has been carried out on parts of the  $H_2$  spectrum using MQDT. Two representative cases will be discussed: Rotational autoionization, and a prediction of vibrational branching ratios and photoelectron angular distributions resulting from vibrational autoionization above the  $v^+=3$  limit at  $\sim 764.8$  Å. These predictions have not yet been tested, although equivalent experiments on electronic autoionization in  $N_2$  have recently been performed [168,169]. These latter results will constitute our example of experimental progress. In Section 3.4 we summarize the progress and prospects in this area, emphasizing that while experiment and theory are approaching one another, it is crucial that this progress converge to direct tests at the triply-differential level as soon as possible.

### 3.2 MQDT Treatment of Autoionization in $H_2$

Multichannel quantum defect theory and its application to molecular photoionization have been described in detail elsewhere [137-150], including elsewhere in this volume. Hence, we only briefly summarize the important attributes of MQDT and then turn to two examples of its application to photoionization in  $H_2$ .

MQDT is a theoretical framework which *simultaneously* treats the interactions between and within *whole* excitation channels. The input to an MQDT calculation consists chiefly of a small set of physically meaningful parameters (quantum defects and dipole amplitudes) which characterize the short-range interactions between the excited electron and the core, are slowly-varying functions of energy relative to rovibronic structure in the spectrum, and can generally be obtained from the positions and intensities of low-lying states in the spectrum. Also used are known transformation properties of molecular wavefunctions, e.g., transformations between Hund's coupling cases, and the asymptotic bound-

any conditions pertinent to a particular spectral range. Given this input, straightforward matrix mechanics yields, at each excitation energy, the spectral composition of the total final-state wavefunction in terms of the short-range, body-frame basis set, known dipole strengths and the asymptotic eigenphase shifts of the observable ionization channels. These quantities are then related, by now standard formulas, to such observables as the total photoionization cross-section, vibrational branching ratios and photoelectron angular distributions.

We wish to emphasize that this theoretical framework is not only elegant, but also reflects very accurately the internal mechanics of the excited complex. Hence, the quality of the computed observable depends solely upon the quality of the input. When accurate, empirical quantum defects are used, adiabatic and nonadiabatic corrections to the Born-Oppenheimer approximation are included automatically, to all orders. Hence, given physical input from low-lying excited states, one can use MQDT to generate accurate predictions for experiments throughout the extremely complex high-excitation regions. This is to be contrasted to the normal perturbation approach, which would require treating each state separately, with explicit adiabatic and non-adiabatic corrections and with little hope of treating higher-order interactions within and between whole excitation channels.

A striking example of the power and accuracy of MQDT in a complex situation is provided by the rich, rotational/vibrational autoionization structure in the  $174.3 \text{ cm}^{-1}$  spectral range between the  $N^+=0$  and 2 rotational thresholds associated with the lowest  $v^+=0$  ionization potential of  $\text{H}_2$ . The results of a calculation [144] of this structure are given in Fig. 20. The level positions indicated across the top of the figure are those one obtains with discrete boundary conditions (i.e., by eliminating open channels from the linear system). This level of analysis determines the initial assignments of spectral features. Alternatively, photoabsorption directly into the continuum is shown across the bottom of Fig. 20. This represents the single-channel level of approximation used throughout the discussion of shape resonances in Section 2. If rotational autoionizing channels only are introduced, the np2 levels of the Rydberg series converging to the upper ( $N^+=2$ ) threshold of  $\text{H}_2^+ \times 2\Sigma_g^+$  ( $v^+=0$ ) autoionize and distort the continuum into a Rydberg series of Fano-Beutler profiles. This is shown in the middle frame of Fig. 20. Finally, if vibrational autoionization channels are also introduced, the  $5p\pi(v=2)$  and  $7p\pi(v=1)$  levels autoionize and strongly distort the rotationally autoionizing levels as well, shifting intensity from above to below the vibrational interlopers.

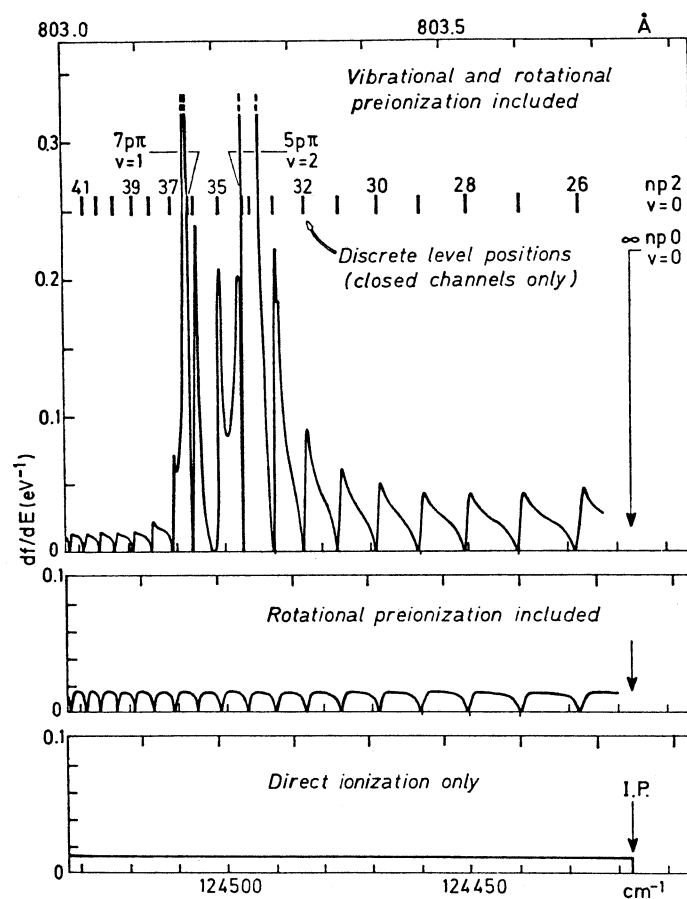


Fig. 20. MQDT calculation of photoionization of  $\text{H}_2$   $X\ 1\Sigma_g^+$  ( $J'' = 0$ ,  $v'' = 0$ ) near the ionization threshold (taken from [144]).

We see, therefore, that the effect of vibrational autoionization on the ionization cross-section is profound, and that it affects the whole range shown (corresponding to  $\sim 100\text{ cm}^{-1}$ ). Indeed, if the fine variations in the cross-section are neglected, the whole spectrum can be viewed as one "giant" resonance of  $\sim 50\text{ cm}^{-1}$  width, which causes a global transfer of intensity from the high-energy to the low-energy side of the vibrational peaks. This transfer leads to further modifications of the fine structure. For example, for  $n=26$  and  $27$  the intensity minima still correspond nearly to the discrete  $np2$  levels; for higher  $n$ , however, the profiles become progressively distorted until, near  $n=$

32 to 35, it is the intensity maxima which coincide with the discrete level positions. In other words, there no longer exists a simple relationship between the extrema of the ionization curve and the positions of the autoionizing levels. In view of these complexities, it is clear that vibrational and rotational autoionization cannot be meaningfully treated as separate processes in this spectral region. A key feature of MQDT, however, is that it is based on no such assumed separability, i.e., it

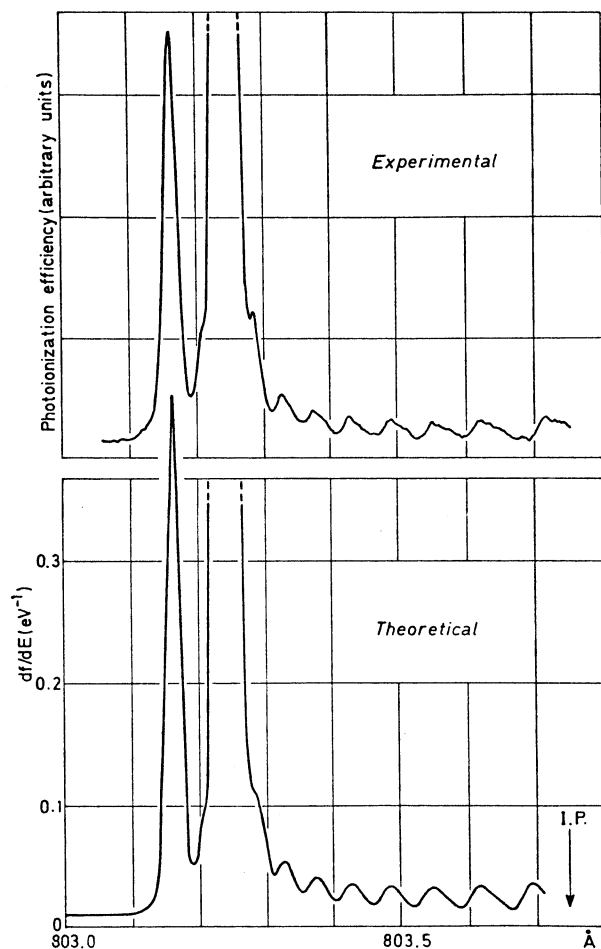


Fig. 21. MQDT results from Fig. 20, broadened to a resolution of 0.022 Å and compared with data from [220] (taken from [144]).

is applicable independently of coupling strengths between alternative decay mechanisms.

In Fig. 21, the calculated spectrum is compared with the high-resolution photoionization spectrum [220]. The calculated spectrum from Fig. 20 was convoluted with a triangular apparatus function of width 0.022 Å to mimic the finite experimental resolution. The comparison in Fig. 21 shows essentially exact agreement and reflects, more clearly than words, the state-of-the-art in computational simulation of detailed photoionization dynamics.

Triply-differential cross-sections have also been computed [148] near each of the levels shown explicitly in Fig. 17. However, we shall skip to the highest set of levels, above the  $v^+=3$  limit, to discuss MQDT predictions of vibrational branching ratios and  $\beta$ 's. This spectral range, between 762.5 and 765 Å in Fig. 19, is most attractive for future experimental examination since it produces four photoelectron peaks, corresponding to  $v^+=0-3$ , with sufficiently large photoelectron energies to be measured with existing electron-energy analyzers.

Fig. 22 shows the calculated total and vibrational partial cross-sections (the rotational sublevels have been summed over) in this spectral range, together with total photoionization data [220]. In this case the calculations are not folded with the instrument function and are, accordingly, sharper and higher. The horizontal arrow indicates the height that would be obtained from such a convolution. Also, the vertical arrows show more precise peak positions from the high-resolution absorption spectrum [139]. Given these qualifications, the agreement in the total cross-section is, again, quite satisfactory. The vibrational partial cross-sections, for which no experimental data are available, are shown at the bottom of Fig. 22. There, we see that the widths of the vibrational autoionization peaks are the same as in the total cross-section, as expected, but that the profiles vary drastically. Other details of the behavior of these partial cross-sections are displayed more clearly in the vibrational branching ratios, discussed below.

Fig. 23 again shows the total photoionization cross-section, together with the total  $\beta$  (summed over  $v^+$ ) and includes the vibrational branching ratio and  $\beta_{v^+}$  for each vibrational ionization channel  $v^+$ . The total  $\beta$  curve is observed to dip strongly within the resonances. This is a consequence of the discrete wavefunction component mixing strongly into the ionization continuum. Classically speaking, one would say that the "quasibound" photoelectron spends more time near the core so that angular momentum exchange is enhanced. In this case the  $N^+=2$  ionization channel becomes dominant near the center of the re-

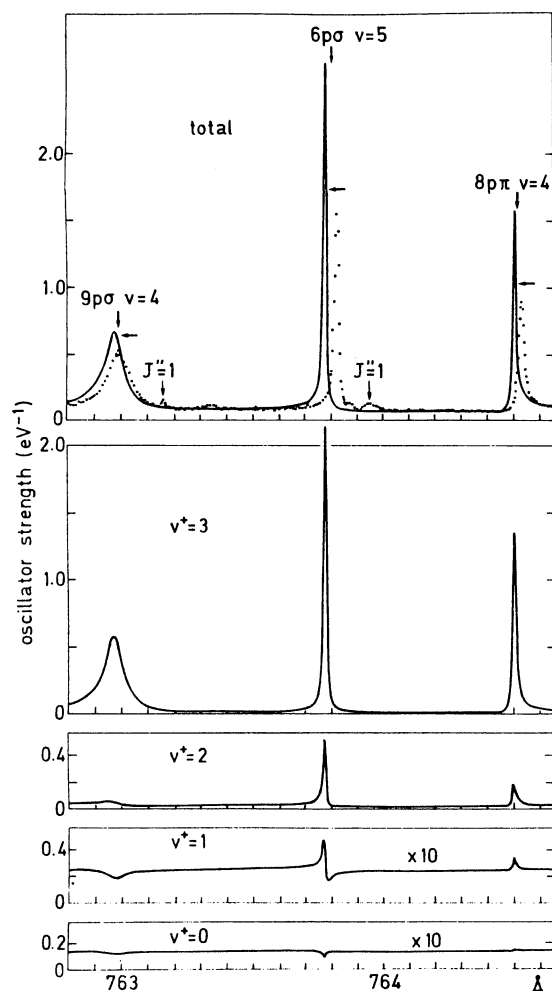


Fig. 22. Total and partial oscillator strengths for photoionization of  $\text{H}_2$  near the  $v^+ = 3, N^+ = 2$  ionization threshold (764.755  $\text{\AA}$ ). Experimental points from [220]; figure taken from [148].

sonance and the value of  $\beta$  is depressed correspondingly, showing that directional information carried by the incoming photon is largely transferred to molecular rotation in the subsequent electron-core collisions. This general behavior is also reflected in the partial  $\beta_{v^+}$  curves although, in addition, a strong  $v^+$  dependence in the magnitudes and shapes of these curves is

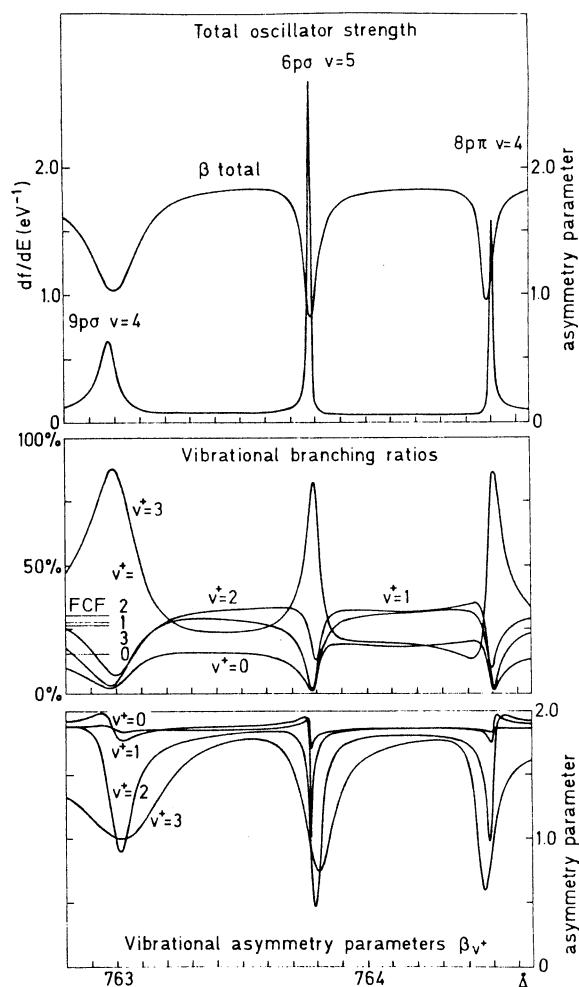


Fig. 23. Asymmetry parameter  $\beta$  (total and vibrationally-resolved) and vibrational branching ratios for photoionization of  $H_2$  near the  $v^+ = 3$ ,  $N^+ = 2$  ionization threshold (764.755 Å). Figure taken from [148].

observed. Note that the spectral extent of the variations induced in  $\beta_{v^+}$  by vibrational autoionization is considerably larger than the halfwidths of the resonances themselves. This is a significant advantage in triply-differential experimental studies, which are difficult to perform with narrow photon bandwidth, for intensity reasons, and are only now being planned

with bandwidths of 0.1-0.2 Å.

The middle frame in Fig. 23 shows the vibrational branching ratios in this energy region, along with the FC factors for direct ionization. As in the case of shape-resonant photoionization, striking non-FC behavior is observed in the vicinity of the vibrationally autoionizing states. And, as observed for  $\beta_{v^+}$ , the spectral extent of the autoionization effects is greater than the autoionizing resonance halfwidth, when displayed in terms of vibrational branching ratios, an observation which is significant in the context of experimental tests of these predictions. These calculations also predict that the branching ratio in the open channel possessing the highest  $v^+$  (corresponding to autoionization with the lowest possible  $|\Delta v|$ ) is strongly enhanced at the expense of all other channels, which are strongly depressed from their FC factors. Thus, the well-known qualitative rule [229], which states that a vibrationally-autoionized level decays preferentially with the smallest possible change of vibrational quantum number, is globally confirmed in these calculations, although for certain wavelengths (e.g., 764.4 Å in Fig. 23) the exact opposite may be true.

The above results tend to lull one into the feeling that we understand photoionization in  $H_2$  completely, needing only to extend the range of the MQDT treatment to any energy region of

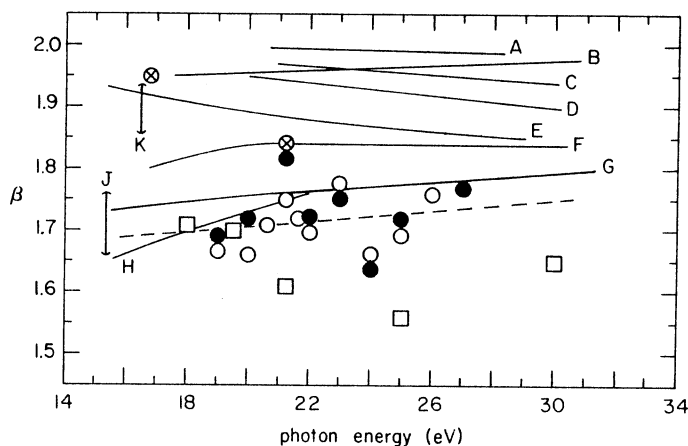


Fig. 24. Various experimental and theoretical results for the asymmetry parameter,  $\beta$ , for photoionization of  $H_2$  and  $D_2$ . Complete citations for the various data are given in [232], from which this figure was taken.

interest. Nevertheless, it is imperative to perform experimental tests at the triply-differential level since it is in the more detailed quantities, such as vibrational branching ratios and angular distributions, that we are most likely to observe shortcomings in our detailed understanding of this important fundamental system. That such measurements have *not* been performed is often surprising to some. To emphasize the dearth of detailed data on this point, we show, in Fig. 24, a recent summary [232] of  $\beta$  measurements on  $H_2$  (and  $D_2$ ), together with other theoretical treatments. The gap between Figs. 23 and 24 is enormous. Indeed, the measurements are difficult; however, optimization of current technology should make this goal attainable. This is, one of the main motivations for the new-generation instrument described in Section 2.3b.

### 3.3 Triply-Differential Measurements Within Autoionization Resonances

Recall the scattered data in the  $15.5 \text{ eV} \leq h\nu \leq 20 \text{ eV}$  region of the vibrational branching ratio results for  $N_2$  (cf. Fig. 15). As indicated in the discussion of these data, the scatter was

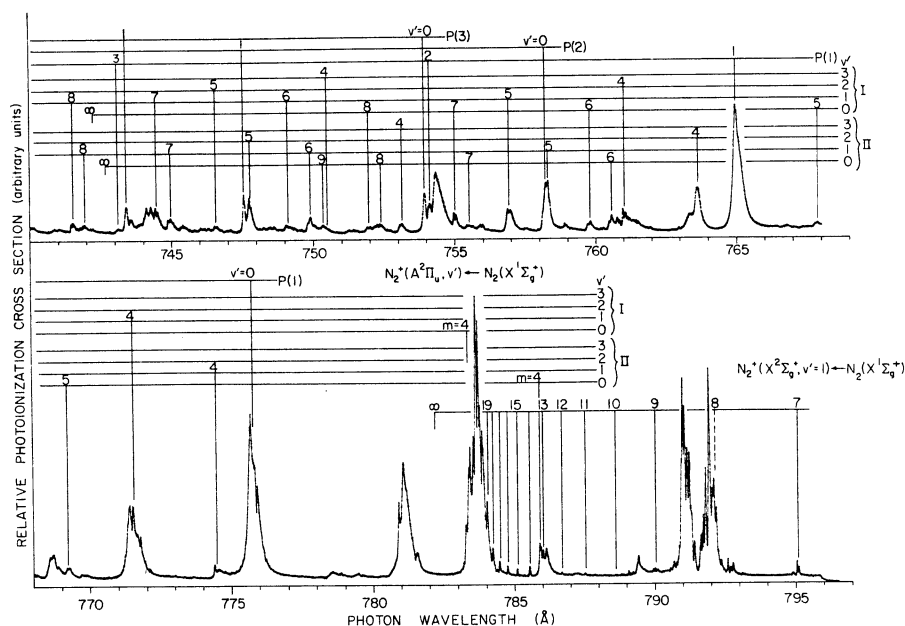


Fig. 25. A portion of the photoionization spectrum of  $N_2$  at  $78^\circ K$  (taken from [222]).

produced by unresolved autoionization structure leading to the A and B states of  $N_2^+$  (see Fig. 8). The high-resolution, total photoionization spectrum [222] of  $N_2$  in that spectral range is given in Figs. 25 and 26, showing the rich autoionization structure in the  $N_2$  spectrum. This structure serves to emphasize the difference in precision needed in studying the two types of resonant photoionization processes --- shape resonances and autoionizing resonances. The relatively broad Hopfield absorption and emission Rydberg series [233], converging to the  $v=0$  level of  $N_2^+ B^2\Sigma_u^+$  at 661.2 Å, was chosen for the initial triply-differential study [168] of molecular autoionization structure. This choice was guided by two considerations: First, this series represents a relatively isolated Rydberg series, the lower members of which are sufficiently broad to permit a systematic, detailed investigation of autoionization profiles with available instrumentation. Second, this was considered a good prototype for investigating the full rotational-vibrational-electronic interplay in the autoionization process. In this example, the autoionizing states consist of a Rydberg electron bound to an electronically excited  $N_2^+ B^2\Sigma_u^+$  ( $v=0$ ) core. Ionization occurs when the Rydberg electron collides with the core, thus enabling an exchange of the large electronic excitation energy of the core, together with smaller amounts of energy from the nuclear

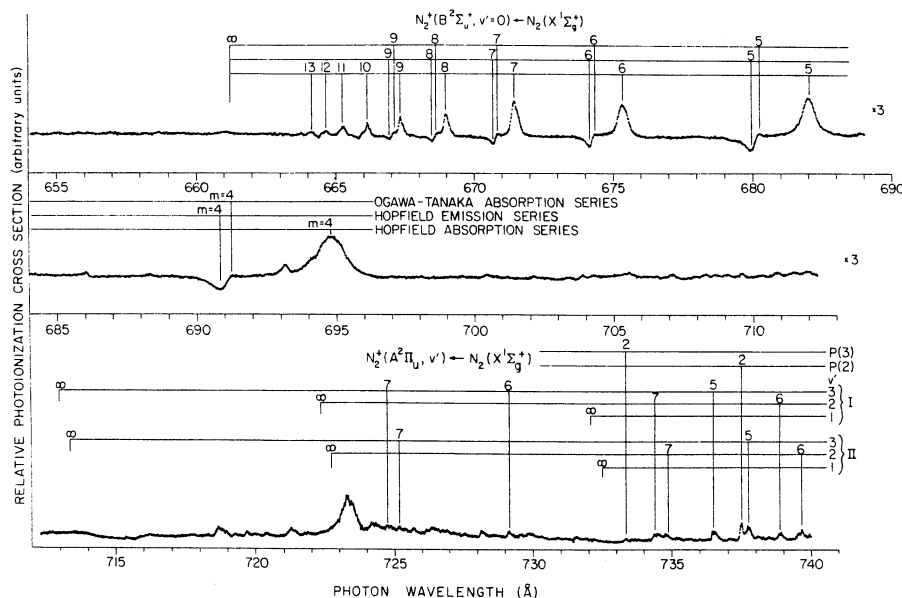


Fig. 26. A portion of the photoionization spectrum of  $N_2$  at 78°K (taken from [222]).

modes.

Although several members of the Hopfield absorption and emission series have been studied [169] by triply-differential photoelectron spectroscopy, we focus here on the lowest (and broadest)  $m=3$  members of these series at  $\lambda = 723.3 \text{ \AA}$  (absorption) and  $715.5 \text{ \AA}$  (emission). The spectroscopic assignments for these series are summarized elsewhere [168]. We note, however, that the window and main absorption series, together with a weaker absorption series occurring between them, seem to be most consistent with the designations  $nd\pi_g$ ,  $nd\sigma_g$  and  $ns\sigma_g$ , although these assignments have not been unequivocally established.

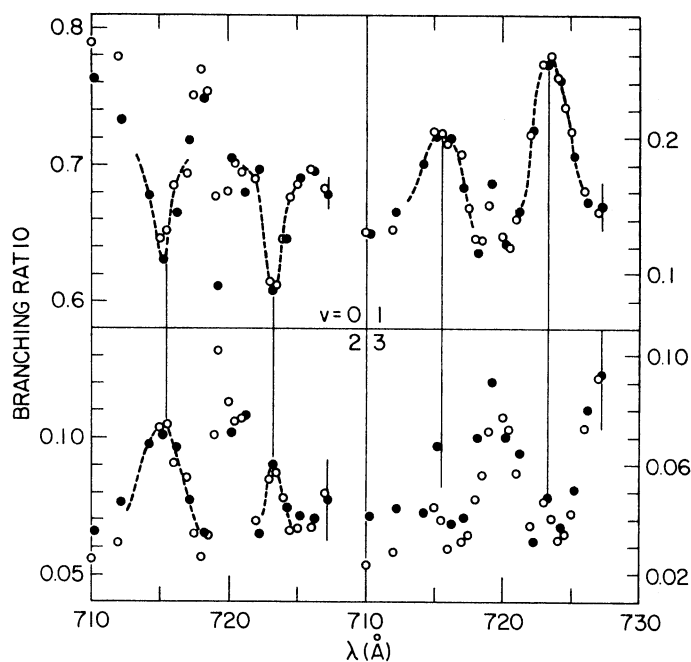


Fig. 27. Vibrational branching ratios for production of  $N_2^+ X \ 2\Sigma_g^+$  ( $v = 0-3$ ) in the range  $710 \text{ \AA} \leq \lambda \leq 730 \text{ \AA}$ . Vertical lines at  $715.5$  and  $723.3 \text{ \AA}$  denote the positions of the first members of the Hopfield "emission" and absorption series approaching the  $N_2^+ B \ 2\Sigma_u^+$  ( $v = 0$ ) limit. Typical error bars are indicated on the last point in each frame. The dashed line is hand drawn to guide the reader's eye. Open and closed circles represent two independent runs. Figure taken from [168].

In Fig. 27, we present the vibrational branching ratios for formation of the ground-state ion  $N_2^+ X 2\Sigma_g^+$  by photoionization in the range  $710 \text{ \AA} \leq \lambda \leq 730 \text{ \AA}$ . (Here we define the vibrational branching ratio as the ratio of the intensity of a particular vibrational level to the sum over the whole vibrational band.) In Fig. 28, the asymmetry parameter  $\beta$  is given for the same processes. In both figures, the positions of the Hopfield emission and absorption features at  $715.5 \text{ \AA}$  and  $723.3 \text{ \AA}$ , respectively, are indicated by solid lines joining the upper and low-

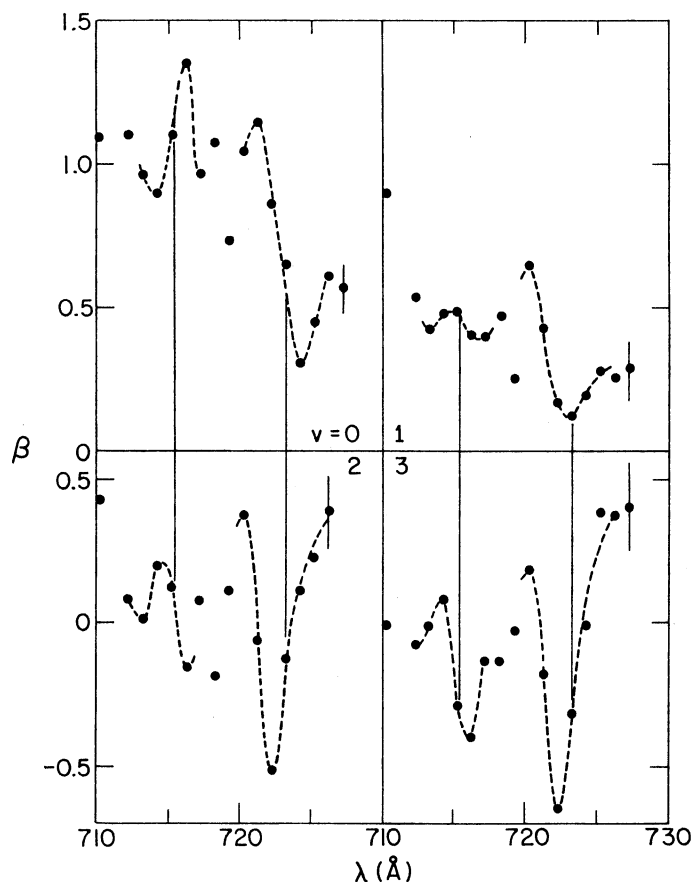


Fig. 28. Photoelectron asymmetry parameters corresponding to producing  $N_2^+ X 2\Sigma_g^+$  ( $v = 0-3$ ) in the range  $710 \text{ \AA} \leq \lambda \leq 730 \text{ \AA}$ . Other conventions as in Fig. 27. Figure taken from [168].

er frames. In the vicinity of these features, a hand-drawn dashed curve is constructed only to guide the eye and should not be taken too seriously. Typical error bars for the data in both figures are shown on the last point in each frame. Duplicate branching-ratio measurements (the open circles were taken at the magic angle and the solid dots were deduced from the angular distribution measurements) show the reproducibility of the data. Note that an early branching-ratio study of this region of the  $N_2$  photoionization spectrum was reported by Woodruff and Marr [164,165], but without angle dependence and with insufficient wavelength resolution to characterize the profiles of the Hopfield resonances.

Focusing first on the vibrational branching ratios in Fig. 27, we see three major qualitative features:

(i) The  $v=0$  branching ratio exhibits pronounced dips at the locations of the two major autoionization features, whereas the higher vibrational channels, most notably  $v=1$ , show enhancements. Hence, the quasibound autoionizing states mediate a transfer of dipole amplitude from the  $v=0$  channel to the much weaker  $v=1,2$  and 3 channels, a transfer which involves simultaneous electronic deexcitation and vibrational excitation of the ion core. This transfer is primarily directed to the  $v=1$  channel and is much diminished by  $v=3$ . Such an enhancement of vibrational channels possessing small Franck-Condon factors relative to the most intense channel is reminiscent of the effects of shape resonances in those few cases studied so far. Comparison with vibrational autoionization in  $H_2$ , where ionization channels with the minimum (negative)  $\Delta v$  usually dominate [148,229], is not straightforward since  $\Delta v=0$  is permitted in this case; and, at any rate, transitions in which vibrational excitation occurs are favored. Establishing the systematics of this diverse set of observations is, obviously, a most timely problem.

(ii) Despite the great contrast between window and absorption profiles in the photoabsorption and photoionization spectra, the profile in Fig. 27 are of similar shape and both exhibit either an enhancement or depletion, depending upon the channel.

(iii) Definite "interloper" structure occurs between the two major resonances, with variable shape and strength. Both the weak absorption peak near the window resonances and other weak structures (one peak in the photoionization spectrum at  $718.8 \text{ \AA}$  correlates well with the main interloper structures in Fig. 27) may play a role here.

The angular distribution results of Fig. 28 also exhibit structure at the positions of the two major resonances and in

between. Implicit in the spectral variations in  $\beta$  is information on both the vibrational branching ratios and the relative phases of the alternative vibrational ionization channels. Specifically, the competition between asymptotic phases produces large asymmetric variations in  $\beta$  at the resonance positions, variations which differ from one final vibrational level to another. For instance, the  $\beta$  curve near the Hopfield "emission" line exhibits a peak for  $v=0$  which evolves into a dip for  $v=3$ . Near the Hopfield absorption profile, the position of the minimum in  $\beta$ , although not extremely well-defined by these data, clearly shifts from the long-wavelength side of the resonance position to the short-wavelength side.

We conclude by observing that, although this example is one of only a few measurements of its kind at this time (see the next section), the experimental developments described in Section 2.3b, and those occurring in other laboratories, will make available more systematic, triply-differential studies in many molecules in the next few years. It is, therefore, most timely to extend calculations, such as those described in Section 3.2, to the full rovibronic description of molecular autoionization, in order to help guide experimental progress and to extract the wealth of detailed dynamical information contained in the anticipated growth of triply-differential data. Fortunately, theoretical progress in this direction is already substantial, as summarized in the next section.

### 3.4 Progress and Prospects

In addition to the prototype  $H_2$  and  $N_2$  cases discussed above, there have been a large number of molecules for which autoionization structure in the total photoionization cross-section has been mapped out (see, e.g., [2,120,214-228]). These spectra contain a great deal of dynamical information in themselves and create an indispensable roadmap for choosing particular cases for detailed study. More recently, additional triply-differential measurements have been performed on broad autoionization features in  $O_2$  [166],  $CO$  [167],  $CO_2$  [170] and  $C_2H_2$  [125,131]. In addition, very detailed vibrationally-resolved partial cross-sections for production of  $O_2^+ B^4\Sigma_g^-$  and  $B^2\Sigma_g^-$  have been measured [132-134] systematically throughout the complex autoionization structure in the  $h\nu = 18-21$  eV range. As mentioned above (Section 2.4), this work addressed, and has rather clearly resolved, the spectroscopy and dynamics arising from overlapping shape and autoionizing resonances in this region, using a combination of experimental and theoretical methods.

Progress on the theoretical side has also been substantial. The MQDT analysis of electronic autoionization in  $O_2$  just mentioned is a good example of utilizing MQDT in a more complicat-

ed situation, where the basic input is not as complete as in the case of  $H_2$  and must, therefore, be approximated or empirically derived. This type of application exploits the powerful theoretical framework of MQDT to reflect complicated dynamics in terms of a few parameters, which can even be deduced by forcing the calculated spectrum to mimic experiment. This permits us to access the information contained in these data, at least until means [150] to compute input parameters for more complicated molecules are adequately developed. Other examples of successful MQDT analyses include NO [149] and  $N_2$  [146, 149]; both of these molecules exhibit a very interesting hybrid autoionization mechanism in which the net result is vibrational autoionization, but for which all of the strength derives from indirect electronic coupling with an interloper converging to a higher electronic threshold.

Clearly, experimental and theoretical programs to probe more deeply into molecular autoionization dynamics are proceeding in a healthy manner. However, special emphasis should be placed on making progress toward the (still missing) direct comparison at the triply-differential level. Technical difficulties exist on both experimental and theoretical sides but the progress cited above would indicate that this prime goal is within present capabilities. To be specific, the shortest path toward a direct comparison would appear to be an experimental test of the theoretical predictions in Fig. 23, and theoretical analyses of the experimental data in Figs. 27 and 28. We expect these and many more examples to emerge in the next few years.

#### 4. CONCLUDING REMARKS

In order to place the preceeding sections in a broader perspective, we briefly indicate how a variety of techniques are presently being used to probe aspects of molecular photoionization dynamics which are complementary to those emphasized here: (i) Multiphoton ionization is a recently developed technique which has a great potential for expanding our understanding of photoionization dynamics in totally new directions. When used in conjunction with photoelectron detection, such as that described in Section 2.3b, vibrational intensities and photoelectron angular distributions can be measured (see, e.g., [234-241]) to provide windows onto the dynamics of the multiphoton process, just as they do in the single-photon case. In addition, when the multiphoton process proceeds via resonances with excited neutral states, such as the excited valence states of  $N_2$  in Fig. 8, very high-resolution ( $\Delta\lambda < 0.05 \text{ cm}^{-1}$ ) spectroscopy and dynamics of these *intermediate* resonances can be examined. (ii) Another recently developed technique [242,243] is polarization of fluorescence from molecular ions formed by photoioniza-

tion. This approach accesses information on the orientation of the molecular ion and the relative strengths of degenerate photoelectron channels in the photoionization process. To give a concrete example, photoionization of  $N_2$  to form the  $B\ ^2\Sigma_u^+$  state of  $N_2^+$  (see Fig. 8) leads to the rightmost photoelectron band in Fig. 9. This band consists of electrons in degenerate  $\epsilon\sigma_g$  and  $\epsilon\pi_g$  ionization channels which cannot be separated by straightforward electron spectroscopy or by  $\beta$  measurements. Nevertheless, by observation of the polarization of the B-X fluorescence, information on the branching ratio for these degenerate photoelectron channels can be obtained [242]. This provides a unique test of dynamical information which exists, but usually remains implicit, in theoretical calculations. This technique has recently been extended [243] to the study of autoionization structure in the photoionization of  $CO_2$ . Another, apparently dissimilar, technique for examining relative strengths of degenerate photoionization channels is the measurement of angular distributions of photoions from dissociative photoionization [244]. The common link between these techniques is that they do not detect (and, hence, integrate over the angular distribution of) the photoelectrons, thus eliminating the interference effects between degenerate channels and isolating their relative strengths in the observed parameters. (iii) An important extension of the triply-differential studies discussed above is the measurement of spin polarization of the photoelectrons. Spin-polarization measurements access additional dynamical information described in detail elsewhere [158]. Full quadruply-differential measurements have already been performed on atoms [158] and spin-polarization measurements have been made on molecules [245]. (iv) A variety of dissociative phenomena occur either in competition with or subsequent to molecular photoionization, and are an important part of the broader picture. For example, MQDT has been applied [149] to the competition between predissociation and autoionization in photoexcitation of NO, an application which represents an extension of MQDT analysis to dissociation channels and thereby serves as a prototype for an extensive class of processes always present to some degree in molecular photoexcitation spectra. Another subject with a rich literature (see, e.g. [246-254]) is fragmentation of molecular ions formed by photoionization. Usually studied by photoelectron-photoion coincidence techniques, this subfield focuses on the decay of excited molecular ions into alternative dissociation channels. (v) A class of phenomena which appear to be very common in inner-valence-shell spectra results from the breakdown of the single-particle model brought on by extensive vibronic coupling among the high density of states in the inner-valence region [211]. This breakdown manifests itself in a high density of satellites in photoelectron spectra (consisting of admixtures of single-hole states, two-hole one-particle states and certain higher-order combinations) to the extent that the main photoelectron

line associated with a single inner-valence hole can even be difficult to recognize. This has been treated successfully, e.g., in the case of the " $2\sigma_u$ " spectrum [91] of  $N_2$ , by many-body Green's function techniques [211], and may be expected to be an important dynamical effect in the photoionization of molecular levels possessing IP's in the  $h\nu \approx 30$ –50 eV range.

In closing, we emphasize that, although extensive, this survey is not at all comprehensive. Hopefully, it does succeed in indicating both the present richness of the field of molecular photoionization dynamics and the opportunities for significant progress in the future.

#### ACKNOWLEDGMENT

This work was supported by the U.S. Department of Energy, the Office of Naval Research, NATO Grant No. 1939, and National Science Foundation Grant CHE-8203267.

#### REFERENCES

1. U. Fano and J. W. Cooper, *Rev. Mod. Phys.* **40**, 441 (1968).
2. E. E. Koch and B. F. Sonntag, in: *Synchrotron Radiation: Techniques and Applications*, C. Kunz, ed. (Springer-Verlag, Heidelberg, 1979), p. 269.
3. A bibliography of inner-shell spectra is given by A. P. Hitchcock, *J. Electron Spectrosc.* **25**, 245 (1982).
4. R. E. LaVilla and R. D. Deslattes, *J. Chem. Phys.* **44**, 4399 (1966).
5. T. M. Zimkina and V. A. Fomichev, *Dokl. Akad. Nauk SSSR* **169**, 1304 (1966) [*Sov. Phys. Dokl.* **11**, 726 (1966)].
6. V. A. Fomichev, *Fiz. Tverd. Tela* **9** 3167 (1971) [*Sov. Phys. Solid State* **9**, 2496 (1968)].
7. M. Nakamura, M. Sasanuma, S. Sato, M. Watanabe, H. Yamashita, Y. Iguchi, A. Ejiri, S. Nakai, S. Yamaguchi, T. Sagawa, Y. Nakai and T. Oshio, *Phys. Rev.* **178**, 80 (1969).
8. T. M. Zimkina and A. C. Vinogradov, *J. Phys. (Paris) Colloq.* **32**, 3 (1971).
9. W. Hayes and F. C. Brown, *J. Phys. B* **4**, L85 (1971).
10. W. Hayes, F. C. Brown and A. B. Kunz, *Phys. Rev. Lett.* **27**, 774 (1971).
11. D. Blechschmidt, R. Haensel, E. E. Koch, U. Nielsen and T. Sagawa, *Chem. Phys. Lett.* **14**, 33 (1972).
12. M. J. van der Wiel and Th. M. El-Sherbini, *Physica (Utrecht)* **59**, 453 (1972).

13. G. R. Wight, C. E. Brion and M. J. van der Wiel, J. Electron Spectrosc. 1, 457 (1972/73).
14. (a) R. E. LaVilla, J. Chem. Phys. 57, 899 (1972); (b) 58, 3841 (1973).
15. G. R. Wight and C. E. Brion, J. Electron Spectrosc. 3, 191 (1974).
16. G. R. Wight and C. E. Brion, J. Electron Spectrosc. 4, 313 (1974).
17. G. R. Wight and C. E. Brion, J. Electron Spectrosc. 4, 327, 335 (1974).
18. V. I. Nefedov, Zh. Strukt. Khim. 11, 292 and 299 (1970) [J. Struct. Chem. 11, 272 and 277 (1970)].
19. V. A. Fomichev and R. L. Barinskii, Zh. Strukt. Khim. 11, 875 (1970) [J. Struct. Chem. 11, 810 (1970)].
20. J. L. Dehmer, J. Chem. Phys. 56, 4496 (1972).
21. F. A. Gianturco, C. Guidotti and U. Lamanna, J. Chem. Phys. 57, 840 (1972).
22. B. Cadioli, U. Pincelli, E. Tosatti, U. Fano and J. L. Dehmer, Chem. Phys. Lett. 17, 15 (1972).
23. U. Fano, Comments At. Mol. Phys. 3, 75 (1972).
24. R. L. Barinskii and I. M. Kulikova, Zh. Strukt. Khim. 14, 372 (1973) [J. Struct. Chem. 14, 335 (1973)].
25. J. L. Dehmer, Phys. Fenn. 9S, 60 (1974).
26. V. P. Sachenko, E. V. Polozhenstev, A. P. Kovtun, Yu. F. Migal, R. V. Vedrinski and V. V. Kolesnikov, Phys. Lett. A 48, 169 (1974).
27. L. N. Mazalov, F. Kh. Gel'mukhanov and V. M. Chermoshentsev, Zh. Strukt. Khim. 15, 1099 (1974) [J. Struct. Chem. 15, 975 (1974)].
28. J. L. Dehmer and D. Dill, Phys. Rev. Lett. 35, 213 (1975).
29. D. Dill, J. Siegel and J. L. Dehmer, J. Chem. Phys. 65, 3158 (1976).
30. J. L. Dehmer and D. Dill, J. Chem. Phys. 65, 5327 (1976).
31. J. W. Davenport, Phys. Rev. Lett. 36, 945 (1976).
32. J. L. Dehmer and D. Dill, in: *Proceedings of the International Conference on Inner Shell Ionization Phenomena-Invited Papers*, W. Mehlhorn and R. Brenn, eds. (Universitat Freiburg, Freiburg 1976), p. 221.
33. M. Nakamura, Y. Morioka, T. Hayaishi, E. Ishiguro and M. Sasanuma, in: *Third International Conference on Vacuum Ultraviolet Radiation Physics*, Y. Nakai, ed. (Physical Society of Japan, Tokyo, 1971), paper 1pA1-6.
34. Th. M. El-Sherbini and M. J. van der Wiel, Physica (Utrecht) 59, 433 (1972).
35. R. E. LaVilla, J. Chem. Phys. 63, 2733 (1975).
36. W. Eberhardt, R. P. Haelbich, M. Iwan, E. E. Koch and C. Kunz, Chem. Phys. Lett. 40, 180 (1976).
37. A. Hammett, W. Stoll and C. E. Brion, J. Electron Spectrosc. 8, 367 (1976).

38. L. C. Lee, R. W. Carlson and D. L. Judge, *J. Phys. B* 9, 855 (1976).
39. J. A. R. Samson and J. L. Gardner, *J. Electron Spectrosc.* 8, 35 (1976).
40. M. Tronc, G. C. King, R. C. Bradford and F. H. Read, *J. Phys. B* 9, L555 (1976).
41. G. R. Wight, M. J. van der Wiel and C. E. Brion, *J. Phys. B* 9, 675 (1976).
42. J. W. Davenport, *Int. J. Quantum Chem. Symp.* 11, 89 (1977).
43. A. P. Hitchcock and C. E. Brion, *J. Electron Spectrosc.* 10, 317 (1977).
44. R. B. Kay, Ph. E. van der Leeuw and M. J. van der Wiel, *J. Phys. B* 10, 2513 (1977).
45. G. C. King, F. H. Read and M. Tronc, *Chem. Phys. Lett.* 52, 50 (1977).
46. E. W. Plummer, T. Gustafsson, W. Gudat and D. E. Eastman, *Phys. Rev. A* 15, 2339 (1977).
47. T. N. Rescigno and P. W. Langhoff, *Chem. Phys. Lett.* 51, 65 (1977).
48. J. A. R. Samson, J. L. Gardner and G. N. Haddad, *J. Electron Spectrosc.* 12, 281 (1977).
49. J. A. R. Samson, G. N. Haddad and J. L. Gardner, *J. Phys. B* 10, 1749 (1977).
50. W. H. E. Schwarz, T. C. Chang and J. P. Connerade, *Chem. Phys. Lett.* 49, 207 (1977).
51. A. Bianconi, H. Peterson, F. C. Brown and R. Z. Bachrach, *Phys. Rev. A* 17, 1907 (1978).
52. C. E. Brion and K. H. Tan, *Chem. Phys.* 34, 141 (1978).
53. F. C. Brown, R. Z. Bachrach and A. Bianconi, *Chem. Phys. Lett.* 54, 425 (1978).
54. D. Dill, S. Wallace, J. Siegel and J. L. Dehmer, *Phys. Rev. Lett.* 41, 1230 (1978); 42, 411 (1979).
55. T. Gustafsson, *Phys. Rev. A* 18, 1481 (1978).
56. T. Gustafsson, E. W. Plummer, D. E. Eastman and W. Gudat, *Phys. Rev. A* 17, 175 (1978).
57. A. P. Hitchcock and C. E. Brion, *Chem. Phys.* 33, 55 (1978).
58. A. P. Hitchcock, C. E. Brion and M. J. van der Wiel, *J. Phys. B* 11, 3245 (1978).
59. P. W. Langhoff, A. E. Orel, T. N. Rescigno and B. V. McKoy, *J. Chem. Phys.* 69, 4689 (1978).
60. D. G. McCoy, J. M. Morton and G. V. Marr, *J. Phys. B* 11, L547 (1978).
61. N. Padial, G. Csanak, B. V. McKoy and P. W. Langhoff, *J. Chem. Phys.* 69, 2992 (1978).
62. T. N. Rescigno, C. F. Bender, B. V. McKoy and P. W. Langhoff, *J. Chem. Phys.* 68, 970 (1978).
63. M. Sasanuma, E. Ishiguro, H. Masuko, Y. Morioka and M. Nakamura, *J. Phys. B* 11, 3655 (1978).

64. T. Baer, P. M. Guyon, I. Nenner, A. Tabche-Fouhaille, R. Botter, L. F. A. Ferreira and T. R. Govers, *J. Chem. Phys.* **70**, 1585 (1979).
65. D. M. Barrus, R. L. Blake, A. J. Burek, K. C. Chambers and A. L. Pregenzer, *Phys. Rev. A* **20**, 1045 (1979).
66. C. E. Brion, K. H. Tan, M. J. van der Wiel and Ph. E. van der Leeuw, *J. Electron Spectrosc.* **17**, 109 (1979).
67. J. L. Dehmer and D. Dill, in: *Electron-Molecule and Photon-Molecule Collisions*, T. Rescigno, V. McKoy and B. Schneider, eds. (Plenum, New York, 1979), p. 225.
68. J. L. Dehmer and D. Dill, in: *Symposium on Electron-Molecule Collisions*, I. Shimamura and M. Matsuzawa, eds. (University of Tokyo Press, Tokyo, 1979), p. 95.
69. J. L. Dehmer, D. Dill and S. Wallace, *Phys. Rev. Lett.* **43**, 1005 (1979).
70. A. P. Hitchcock and C. E. Brion, *J. Electron Spectrosc.* **15**, 401 (1979).
71. A. P. Hitchcock and C. E. Brion, *Chem. Phys.* **37**, 319 (1979).
72. A. P. Hitchcock and M. J. van der Wiel, *J. Phys. B* **12**, 2153 (1979).
73. P. W. Langhoff, A. Gerwer, C. Asaro and B. V. McKoy, *Int. J. Quantum Chem.* **13**, 645 (1979).
74. H. J. Levinson, T. Gustafsson and P. Soven, *Phys. Rev. A* **19**, 1089 (1979).
75. G. V. Marr, J. M. Morton, R. M. Holmes and D. G. McCoy, *J. Phys. B* **12**, 43 (1979).
76. R. Stockbauer, B. E. Cole, D. L. Ederer, J. B. West, A. C. Parr and J. L. Dehmer, *Phys. Rev. Lett.* **43**, 757 (1979).
77. M. Tronc, G. C. King and F. H. Read, *J. Phys. B* **12**, 137 (1979).
78. S. Wallace, D. Dill and J. L. Dehmer, *J. Phys. B* **12**, L417 (1979).
79. T. A. Carlson, M. O. Krause, D. Mehaffy, J. W. Taylor, F. A. Grimm and J. D. Allen, *J. Chem. Phys.* **73**, 6056 (1980).
80. B. E. Cole, D. L. Ederer, R. Stockbauer, K. Codling, A. C. Parr, J. B. West, E. D. Poliakoff and J. L. Dehmer, *J. Chem. Phys.* **72**, 6308 (1980).
81. J. L. Dehmer and D. Dill, in: *Electronic and Atomic Collisions*, N. Oda and K. Takayanagi, eds. (North-Holland, Amsterdam, 1980), p. 195.
82. D. Dill, J. R. Swanson, S. Wallace and J. L. Dehmer, *Phys. Rev. Lett.* **45**, 1393 (1980).
83. H. Friedrich, B. Pittel, P. Rabe, W. H. E. Schwarz and B. Somntag, *J. Phys. B* **13**, 25 (1980).
84. A. Gerwer, C. Asaro, B. V. McKoy and P. W. Langhoff, *J. Chem. Phys.* **72**, 713 (1980).
85. F. A. Grimm, T. A. Carlson, W. B. Dress, P. Agron, J. O. Thomson and J. W. Davenport, *J. Chem. Phys.* **72**, 3041 (1980).

86. T. Gustafsson, Chem. Phys. Lett. 75, 505 (1980).
87. A. P. Hitchcock and C. E. Brion, J. Electron Spectrosc. 18, 1 (1980).
88. A. P. Hitchcock and C. E. Brion, J. Electron Spectrosc. 19, 231 (1980).
89. A. P. Hitchcock, C. E. Brion and M. J. van der Wiel, Chem. Phys. 45, 461 (1980).
90. R. M. Holmes and G. V. Marr, J. Phys. B 13, 945 (1980).
91. S. Krummacher, V. Schmidt and F. Wuilleumier, J. Phys. B 13, 3993 (1980).
92. P. W. Langhoff, T. N. Rescigno, N. Padial, G. Csanak and B. V. McKoy, J. Chim. Phys. 77, 589 (1980).
93. P. Morin, I. Nenner, P. M. Guyon, O. Dutuit and K. Ito, J. Chim. Phys. 77, 605 (1980).
94. G. Raseev, H. Le Rouzo and H. Lefebvre-Brion, J. Chem. Phys. 72, 5701 (1980).
95. B. Ritchie and B. R. Tambe, J. Phys. B 13, L225 (1980).
96. J. R. Swanson, D. Dill and J. L. Dehmer, J. Phys. B 13, L231 (1980).
97. M. Tronc, G. C. King and F. H. Read, J. Phys. B 13, 999 (1980).
98. S. Wallace, Ph.D. thesis, Boston University (1980).
99. J. B. West, A. C. Parr, B. E. Cole, D. L. Ederer, R. Stockbauer and J. L. Dehmer, J. Phys. B 13, L105 (1980).
100. T. A. Carlson, M. O. Krause, F. A. Grimm, J. D. Allen, D. Mehaffy, P. R. Keller and J. W. Taylor, J. Chem. Phys. 75, 3288 (1981).
101. T. A. Carlson, M. O. Krause, F. A. Grimm, J. D. Allen, D. Mehaffy, P. R. Keller and J. W. Taylor, Phys. Rev. A 23, 3316 (1981).
102. F. A. Grimm, J. D. Allen, T. A. Carlson, M. O. Krause, D. Mehaffy, P. R. Keller and J. W. Taylor, J. Chem. Phys. 75, 92 (1981).
103. T. Gustafsson and H. J. Levinson, Chem. Phys. Lett. 78, 28 (1981).
104. A. P. Hitchcock and C. E. Brion, J. Electron Spectrosc. 22, 283 (1981).
105. P. W. Langhoff, S. R. Langhoff, T. N. Rescigno, J. Schirmer, L. S. Cederbaum, W. Domcke and W. von Niessen, Chem. Phys. 58, 71 (1981).
106. P. W. Langhoff, B. V. McKoy, R. Unwin and A. M. Bradshaw, Chem. Phys. Lett. 83, 270 (1981).
107. D. Loomba, S. Wallace, D. Dill and J. L. Dehmer, J. Chem. Phys. 75, 4546 (1981).
108. R. R. Lucchese and B. V. McKoy, J. Phys. Chem. 85, 2166 (1981).
109. R. R. Lucchese and B. V. McKoy, J. Phys. B 14, L629 (1981).
110. N. Padial, G. Csanak, B. V. McKoy and P. W. Langhoff, Phys. Rev. A 23, 218 (1981).

111. G. Raseev, H. Lefebvre-Brion, H. Le Rouzo and A. L. Roche, *J. Chem. Phys.* 74, 6686 (1981).
112. J. A. Stephens, D. Dill and J. L. Dehmer, *J. Phys. B* 14, 3911 (1981).
113. J. R. Swanson, D. Dill and J. L. Dehmer, *J. Phys. B* 14, L207 (1981).
114. J. R. Swanson, D. Dill and J. L. Dehmer, *J. Chem. Phys.* 75, 619 (1981).
115. A. Tabche-Fouhaille, I. Nenner, P. M. Guyon and J. Delwiche, *J. Chem. Phys.* 75, 1129 (1981).
116. R. Unwin, I. Khan, N. V. Richardson, A. M. Bradshaw, L. S. Cederbaum and W. Domcke, *Chem. Phys. Lett.* 77, 242 (1981).
117. T. A. Carlson, M. O. Krause and F. A. Grimm, *J. Chem. Phys.* 77, 1701 (1982).
118. J. J. Delaney, I. H. Hillier and V. R. Saunders, *J. Phys. B* 15, 1477 (1982).
119. P. M. Dittman, D. Dill and J. L. Dehmer, *J. Chem. Phys.* 76, 5703 (1982).
120. T. Hayaishi, S. Iwata, M. Sasanuma, E. Ishiguro, Y. Morioka, Y. Iida and M. Nakamura, *J. Phys. B* 15, 79 (1982).
121. E. Ishiguro, S. Iwata, Y. Suzuki, A. Mikuni and T. Sasaki, *J. Phys. B* 15, 1841 (1982).
122. R. R. Lucchese and B. V. McKoy, *Phys. Rev. A* 26, 1406 (1982).
123. R. R. Lucchese, G. Raseev and B. V. McKoy, *Phys. Rev. A* 25, 2572 (1982).
124. L. E. Machado, E. P. Leal, G. Csanak, B. V. McKoy and P. W. Langhoff, *J. Electron Spectrosc.* 25, 1 (1982).
125. A. C. Parr, D. L. Ederer, J. B. West, D. M. P. Holland and J. L. Dehmer, *J. Chem. Phys.* 76, 4349 (1982).
126. S. H. Southworth, C. M. Truesdale, P. Kobrin, D. Lindle, W. D. Brewer and D. A. Shirley, *J. Chem. Phys.* 76, 143 (1982).
127. S. Wallace, D. Dill and J. L. Dehmer, *J. Chem. Phys.* 76, 1217 (1982).
128. C. E. Brion and K. H. Tan, *J. Electron Spectrosc.* 23, 1 (1981).
129. J. L. Dehmer, A. C. Parr, S. Wallace and D. Dill, *Phys. Rev. A* 26, 3283 (1982).
130. P. M. Dittman, D. Dill and J. L. Dehmer, *Chem. Phys.*, in press.
131. P. R. Keller, D. Mehaffy, J. W. Taylor, F. A. Grimm and T. A. Carlson, *J. Electron Spectrosc.* 27, 223 (1982).
132. P. Morin, I. Nenner, M. Y. Adam, M. J. Hubin-Franskin, J. Delwiche, H. Lefebvre-Brion and A. Giusti-Suzor, *Chem. Phys. Lett.*, in press.
133. P. Morin, I. Nenner, P. M. Guyon, L. F. A. Ferreira and K. Ito, *Chem. Phys. Lett.*, in press.

134. I. Nenner, P. Morin, L. F. A. Ferreira, P. M. Guyon, K. Ito, K. Kollman and O. Dutuit, to be published.
135. D. Dill and J. L. Dehmer, *J. Chem. Phys.* **61**, 692 (1974).
136. P. W. Langhoff, in: *Electron-Molecule and Photon-Molecule Collisions*, T. N. Rescigno, B. V. McKoy and B. Schneider, eds. (Plenum, New York, 1979), p. 183.
137. U. Fano, *Phys. Rev. A* **2**, 353 (1970).
138. D. Dill, *Phys. Rev. A* **6**, 160 (1972).
139. G. Herzberg and Ch. Jungen, *J. Mol. Spec.* **41**, 425 (1972).
140. O. Atabek, D. Dill and Ch. Jungen, *Phys. Rev. Lett.* **33**, 123 (1974).
141. U. Fano, *J. Opt. Soc. Am.* **65**, 979 (1975).
142. Ch. Jungen and O. Atabek, *J. Chem. Phys.* **66**, 5584 (1977).
143. D. Dill and Ch. Jungen, *J. Phys. Chem.* **84**, 2116 (1980).
144. Ch. Jungen and D. Dill, *J. Chem. Phys.* **73**, 3338 (1980).
145. Ch. Jungen, *J. Chim. Phys.* **77**, 27 (1980).
146. A. Giusti-Suzor and H. Lefebvre-Brion, *Chem. Phys. Lett.* **76**, 132 (1980).
147. M. Raoult, Ch. Jungen and D. Dill, *J. Chim. Phys.* **77**, 599 (1980).
148. M. Raoult and Ch. Jungen, *J. Chem. Phys.* **74**, 3388 (1981).
149. A. Giusti-Suzor, in: *Electronic and Atomic Collisions*, S. Datz, ed. (North-Holland, Amsterdam, 1982), p. 381.
150. G. Raseev and H. Le Rouzo, *Phys. Rev. A* **27**, 268 (1983).
151. *Synchrotron Radiation: Techniques and Applications*, C. Kunz, ed. (Springer-Verlag, Berlin, 1979).
152. *Synchrotron Radiation Research*, H. Winick and S. Doniach, eds. (Plenum, New York, 1980).
153. V. Schmidt, *App. Opt.* **19**, 4080 (1980).
154. E. M. Rowe, *Physics Today* **34**(5), 28 (1981).
155. F. J. Wuilleumier, in: *Atomic Physics*, vol. 7, D. Kleppner and F. M. Pipkin, eds. (Plenum, New York, 1981), p. 491.
156. R. P. Madden and A. C. Parr, *App. Opt.* **21**, 179 (1982).
157. M. G. White, R. A. Rosenberg, G. Gabor, E. D. Poliakoff, G. Thornton, S. H. Southworth and D. A. Shirley, *Rev. Sci. Instrum.* **50**, 1268 (1979).
158. U. Heinzmann, *App. Opt.* **19**, 4086 (1980).
159. A. C. Parr, R. Stockbauer, B. E. Cole, D. L. Ederer, J. L. Dehmer and J. B. West, *Nucl. Instr. Meth.* **172**, 357 (1980).
160. M. O. Krause, T. A. Carlson and P. R. Woodruff, *Phys. Rev. A* **24**, 1374 (1981).
161. H. Derenbach, R. Malutzki and V. Schmidt, *Nucl. Instr. Meth.* **208**, 845 (1983).
162. P. Morin, M. Y. Adam, I. Nenner, J. Delwiche, M. J. Hubin-Franskin and P. Lablanquie, *Nucl. Instr. Meth.* **208**, 761 (1983).
163. A. C. Parr, S. H. Southworth, J. L. Dehmer and D. M. P. Holland, *Nucl. Instr. Meth.* **208**, 767 (1983).

- 164. G. V. Marr and P. R. Woodruff, J. Phys. B 9, L377 (1976).
- 165. P. R. Woodruff and G. V. Marr, Proc. R. Soc. Lond. A 358, 87 (1977).
- 166. K. Codling, A. C. Parr, D. L. Ederer, R. Stockbauer, J. B. West, B. E. Cole and J. L. Dehmer, J. Phys. B 14, 657 (1981).
- 167. D. L. Ederer, A. C. Parr, B. E. Cole, R. Stockbauer, J. L. Dehmer, J. B. West and K. Codling, Proc. R. Soc. Lond. A 378, 423 (1981).
- 168. A. C. Parr, D. L. Ederer, B. E. Cole, J. B. West, R. Stockbauer, K. Codling and J. L. Dehmer, Phys. Rev. Lett. 46, 22 (1981).
- 169. J. B. West, K. Codling, A. C. Parr, D. L. Ederer, B. E. Cole, R. Stockbauer and J. L. Dehmer, J. Phys. B 14, 1791 (1981).
- 170. A. C. Parr, D. L. Ederer, J. L. Dehmer and D. M. P. Holland, J. Chem. Phys. 77, 111 (1982).
- 171. P. H. Doolittle and R. I. Schoen, Phys. Rev. Lett. 14, 348 (1965).
- 172. J. Berkowitz and W. A. Chupka, J. Chem. Phys. 51, 2341 (1969).
- 173. J. E. Collin and P. J. Natalis, Int. J. Mass Spectrom. Ion Phys. 2, 231 (1969).
- 174. J. L. Bahr, A. J. Blake, J. H. Carver, J. L. Gardner and V. Kumar, J. Quant. Spectrosc. Radiat. Transfer 11, 1839 (1971); 11, 1853 (1971); 12, 59 (1972).
- 175. T. A. Carlson, Chem. Phys. Lett. 9, 23 (1971).
- 176. J. L. Gardner and J. A. R. Samson, J. Electron Spectrosc. 2, 153 (1973).
- 177. K. Tanaka and I. Tanaka, J. Chem. Phys. 59, 5042 (1973).
- 178. J. L. Gardner and J. A. R. Samson, Chem. Phys. Lett. 26, 240 (1974).
- 179. G. Caprace, J. Delwiche, P. Natalis and J. E. Collin, Chem. Phys. 13, 43 (1976).
- 180. P. Natalis, J. Delwiche, J. E. Collin, G. Caprace and M. -T. Praet, Chem. Phys. Lett. 49, 177 (1977).
- 181. J. L. Gardner and J. A. R. Samson, J. Electron Spectrosc. 13, 7 (1978).
- 182. J. H. D. Eland, J. Chem. Phys. 72, 6015 (1980).
- 183. V. Kumar and E. Krishnakumar, J. Electron Spectrosc. 22, 109 (1981).
- 184. T. A. Carlson and A. E. Jonas, J. Chem. Phys. 55, 4913 (1971).
- 185. R. Morgenstern, A. Niehaus and M. W. Ruf, in: *Electronic and Atomic Collisions*, L. M. Branscomb, et al., eds. (North-Holland, Amsterdam, 1971), p. 167.
- 186. T. A. Carlson and G. E. McGuire, J. Electron Spectrosc. 1, 209 (1972/73).
- 187. A. Niehaus and M. W. Ruf, Z. Phys. 252, 84 (1972).

188. W. H. Hancock and J. A. R. Samson, *J. Electron Spectrosc.* 9, 211 (1976).
189. D. M. Mintz and A. Kuppermann, *J. Chem. Phys.* 69, 3953 (1978).
190. S. Katsumata, Y. Achiba and K. Kimura, *J. Electron Spectrosc.* 17, 229 (1979).
191. M. H. Kibel, F. J. Leng and G. L. Nyberg, *J. Electron Spectrosc.* 15, 281 (1979).
192. J. Kreile and A. Schweig, *J. Electron Spectrosc.* 20, 191 (1980).
193. J. Kreile, A. Schweig and W. Thiel, *Chem. Phys. Lett.* 79, 547 (1981).
194. J. N. Bardsley and F. Mandl, *Rep. Prog. Phys.* 31, 472 (1968).
195. G. J. Schulz, *Rev. Mod. Phys.* 45, 422 (1973).
196. N. F. Lane, *Rev. Mod. Phys.* 52, 29 (1980).
197. T. Gustafsson and E. W. Plummer, in: *Photoemission and the Electronic Properties of Surfaces*, B. Feuerbacher, B. Fitton and R. F. Willis, eds. (J. Wiley, New York, 1978), p. 353.
198. T. Gustafsson, *Surface Science* 94, 593 (1980).
199. T. Åberg and J. L. Dehmer, *J. Phys. B* 6, 1450 (1973).
200. M. S. Child, *Molecular Collision Theory* (Academic Press, New York, 1974), p. 51.
201. M. Krauss and F. H. Mies, *Phys. Rev. A* 1, 1592 (1970).
202. R. de L. Kronig, *Z. Physik* 70, 317 (1931); 75, 191 (1932).
203. B. Kincaid and P. Eisenberger, *Phys. Rev. Lett.* 34, 1361 (1975).
204. See, for example, R. G. Newton, *Scattering Theory of Waves and Particles* (McGraw-Hill, New York, 1966), p. 457.
205. D. M. Chase, *Phys. Rev.* 104, 838 (1956).
206. D. L. Ederer, B. E. Cole and J. B. West, *Nucl. Instr. Meth.* 172, 185 (1980).
207. J. A. R. Samson and A. F. Starace, *J. Phys. B* 8, 1806 (1975).
208. V. G. Horton, E. T. Arakawa, R. N. Hamm and M. W. Williams, *App. Opt.* 8, 667 (1969).
209. G. V. Marr and J. B. West, *At. Data Nucl. Data Tables* 18, 497 (1976).
210. D. M. P. Holland, A. C. Parr, D. L. Ederer, J. L. Dehmer and J. B. West, *Nucl. Instr. Meth.* 195, 331 (1982).
211. L. S. Cederbaum, W. Domcke, J. Schirmer and W. von Niessen, *Phys. Scr.* 21, 481 (1980).
212. U. Fano, *Nuovo Cimento* 12, 156 (1935).
213. U. Fano, *Phys. Rev.* 124, 1866 (1961).
214. V. H. Dibeler and J. A. Walker, *J. Opt. Soc. Am.* 57, 1007 (1967).
215. V. H. Dibeler and S. K. Liston, *Inorg. Chem.* 7, 1742 (1968).

216. W. A. Chupka and J. Berkowitz, *J. Chem. Phys.* 51, 4244 (1969).
217. V. H. Dibeler and J. A. Walker, *Int. J. Mass Spectrom. Ion Phys.* 11, 49 (1973).
218. K. E. McCulloh, *J. Chem. Phys.* 59, 4250 (1973).
219. P. M. Dehmer and W. A. Chupka, *J. Chem. Phys.* 62, 4525 (1975).
220. P. M. Dehmer and W. A. Chupka, *J. Chem. Phys.* 65, 2243 (1976).
221. J. Berkowitz and J. H. D. Eland, *J. Chem. Phys.* 67, 2740 (1977).
222. P. M. Dehmer and W. A. Chupka, Argonne National Laboratory Report ANL-77-65 (1977), p. 28.
223. P. Gurtler, V. Saile and E. E. Koch, *Chem. Phys. Lett.* 48, 245 (1977).
224. P. M. Dehmer and W. A. Chupka, Argonne National Laboratory Report ANL-78-65 (1978), pp. 4, 10, 13, 19.
225. J. Berkowitz, *Photoabsorption, Photoionization and Photoelectron Spectroscopy* (Academic Press, New York, 1979), Chap. 6.
226. P. M. Dehmer, P. S. Dardi and W. A. Chupka, Argonne National Laboratory Report ANL-79-65, p. 7.
227. Y. Ono, E. A. Osuch and C. Y. Ng, *J. Chem. Phys.* 76, 3905 (1982).
228. C. Y. R. Wu and C. Y. Ng, *J. Chem. Phys.* 76, 4406 (1982).
229. R. S. Berry and S. E. Nielsen, *Phys. Rev. A* 1, 383 and 395 (1970); 4, 865 (1971).
230. C. Duzy and R. S. Berry, *J. Chem. Phys.* 64, 2431 (1976).
231. U. Fano, *Physics Today* 29(9), 32 (1976).
232. S. Southworth, W. D. Brewer, C. M. Truesdale, P. H. Kobrin, D. W. Lindle and D. A. Shirley, *J. Electron Spectrosc.* 26, 43 (1982).
233. J. J. Hopfield, *Phys. Rev.* 35, 1133 (1930); 36, 789 (1930).
234. J. C. Miller and R. N. Compton, *J. Chem. Phys.* 75, 22 (1981).
235. J. C. Miller and R. N. Compton, *J. Chem. Phys.* 75, 2020 (1981).
236. J. H. Glowia, S. J. Riley, S. D. Colson, J. C. Miller and R. N. Compton, *J. Chem. Phys.* 77, 68 (1982).
237. J. Kimman, P. Kruit and M. J. van der Wiel, *Chem. Phys. Lett.* 88, 576 (1982).
238. J. C. Miller, R. N. Compton, T. E. Carney and T. Baer, *J. Chem. Phys.* 76, 5648 (1982).
239. M. G. White, M. Seaver, W. A. Chupka and S. D. Colson, *Phys. Rev. Lett.* 49, 28 (1982).
240. J. C. Miller and R. N. Compton, *Chem. Phys. Lett.* 93, 453 (1982).
241. S. T. Pratt, E. D. Poliakoff, P. M. Dehmer and J. L. Dehmer, *J. Chem. Phys.* 78, 65 (1983).

- 242. E. D. Poliakoff, J. L. Dehmer, D. Dill, A. C. Parr, K. H. Jackson and R. N. Zare, *Phys. Rev. Lett.* 46, 907 (1981).
- 243. E. D. Poliakoff, J. L. Dehmer, A. C. Parr and G. E. Leroi, *J. Chem. Phys.* 77, 5243 (1982).
- 244. J. L. Dehmer and D. Dill, *Phys. Rev. A* 18, 164 (1978).
- 245. U. Heinzmann, B. Osterheld, F. Schafers and G. Schonhense, *J. Phys. B* 14, L79 (1981).
- 246. C. J. Danby and J. H. D. Eland, *Int. J. Mass Spectrom. Ion Phys.* 8, 153 (1972).
- 247. B. Brehm, J. H. D. Eland, R. Frey and A. Kustler, *Int. J. Mass Spectrom. Ion Phys.* 12, 197 (1973).
- 248. R. Stockbauer, *J. Chem. Phys.* 58, 3800 (1973).
- 249. R. Stockbauer and M. G. Inghram, *J. Chem. Phys.* 62, 4862 (1975).
- 250. D. M. Mintz and T. Baer, *J. Chem. Phys.* 65, 2407 (1976).
- 251. R. Stockbauer and M. G. Inghram, *J. Chem. Phys.* 65, 4081 (1976).
- 252. R. Stockbauer, *Int. J. Mass Spectrom. Ion Phys.* 25, 89 (1977).
- 253. T. Baer, in: *Gas Phase Ion Chemistry*, M. T. Bowers, ed. (Academic Press, New York, 1979), Chap. 5.
- 254. R. Stockbauer, *Adv. Mass Spectrom.* 8, 79 (1980).